Icarus 409 (2024) 115852

Contents lists available at ScienceDirect

Icarus

journal homepage: www.elsevier.com/locate/icarus

Research Paper

Field-test performance of an ice-melting probe in a terrestrial analogue environment

Fabian Baader [a,*], Marc S. Boxberg [b], Qian Chen [b], Roger Förstner [c], Julia Kowalski [b], Bernd Dachwald [a]

[a] Faculty of Aerospace Engineering, FH Aachen University of Applied Sciences, Hohenstaufenallee 6, Aachen 52064, Germany
[b] Methods for Model-based Development in Computational Engineering, RWTH Aachen University, Eilfschornsteinstr. 18, Aachen 52062, Germany
[c] Institute of Space Technology & Space Applications, University of the German Federal Armed Forces, Werner-Heisenberg-Weg 39, Neubiberg 85577, Germany

ARTICLE INFO

Dataset link: https://doi.org/10.5281/zenodo.6094866

Keywords:
Experimental techniques
Search for extraterrestrial life
Enceladus
Europa
Exploration
Ice melting probe
Melting efficiency

ABSTRACT

Melting probes are a proven tool for the exploration of thick ice layers and clean sampling of subglacial water on Earth. Their compact size and ease of operation also make them a key technology for the future exploration of icy moons in our Solar System, most prominently Europa and Enceladus. For both mission planning and hardware engineering, metrics such as efficiency and expected performance in terms of achievable speed, power requirements, and necessary heating power have to be known.

Theoretical studies aim at describing thermal losses on the one hand, while laboratory experiments and field tests allow an empirical investigation of the true performance on the other hand. To investigate the practical value of a performance model for the operational performance in extraterrestrial environments, we first contrast measured data from terrestrial field tests on temperate and polythermal glaciers with results from basic heat loss models and a melt trajectory model. For this purpose, we propose conventions for the determination of two different efficiencies that can be applied to both measured data and models. One definition of efficiency is related to the melting head only, while the other definition considers the melting probe as a whole. We also present methods to combine several sources of heat loss for probes with a circular cross-section, and to translate the geometry of probes with a non-circular cross-section to analyse them in the same way. The models were selected in a way that minimizes the need to make assumptions about unknown parameters of the probe or the ice environment.

The results indicate that currently used models do not yet reliably reproduce the performance of a probe under realistic conditions. Melting velocities and efficiencies are constantly overestimated by 15 to 50 % in the models, but qualitatively agree with the field test data. Hence, losses are observed, that are not yet covered and quantified by the available loss models. We find that the deviation increases with decreasing ice temperature. We suspect that this mismatch is mainly due to the too restrictive idealization of the probe model and the fact that the probe was not operated in an efficiency-optimized manner during the field tests. With respect to space mission engineering, we find that performance and efficiency models must be used with caution in unknown ice environments, as various ice parameters have a significant effect on the melting process. Some of these are difficult to estimate from afar.

1. Introduction

Icy moons in the outer Solar System recently attracted great interest due to the putative existence of subglacial oceans that contain salts and minerals through the contact of the water with a silicate mantle or core. In particular, Jupiter's moon Europa and Saturn's moon Enceladus are considered to be potentially habitable (Spencer et al., 2009; Lunine et al., 2015; Pappalardo et al., 2015; Sparks et al., 2017) and also classified as ocean worlds (Nimmo and Pappalardo, 2016).

Ice-melting probes may be a key technology for the subsurface access and the exploration of these icy moons (Ulamec et al., 2007; Winebrenner et al., 2013; Dachwald et al., 2014, 2020, 2023). Such probes have been developed since the 1960s for polar research (Kasser, 1960; Philberth, 1962) and are currently used for deep ice penetration and exploration, as well as for glacial sampling. A comprehensive summary of different probe designs as well as previous research and applications can be found in Talalay (2019). While their typical descent

* Corresponding author.
E-mail address: fabian.baader@alumni.fh-aachen.de (F. Baader).

https://doi.org/10.1016/j.icarus.2023.115852
Received 11 April 2023; Received in revised form 11 October 2023; Accepted 30 October 2023
Available online 3 November 2023

Nomenclature

Melting Probe

a	Side length of the IceMole's cross-sectional area (square) (m)
A	Cross-sectional area (m^2)
F	Force (N)
L	Length of the melting probe (m)
l	Coordinate along the probe in longitudinal direction
m	Mass (kg)
R	Radius of a melting probe's cross-section (m)

Modelling and Analysis

d	Depth below the surface (m)
E	Energy (J)
F^*	Buoyancy-corrected contact force (N)
g	Gravitational acceleration ($m\,s^{-2}$)
J_0, Y_0	Bessel functions of first and second kind
L^*	Critical refreezing length (m)
n, b	Fit constants
P	Power (W)
$\dot{Q}$	Heat flow rate ($J\,s^{-1} = W$)
T	Temperature (K)
s	Distance travelled by melting
t	Time (s)
v	Melting velocity ($m\,s^{-1}$)
z	Depth below ice surface (m)
η	Efficiency

Ice Regime

c_p	Specific heat capacity of the ice ($J\,kg^{-1}\,K^{-1}$)
h	Latent heat of melting (J)
α	$= \lambda/(\rho c_p)$, thermal diffusivity ($m^2\,s^{-1}$)
λ	Thermal conductivity
μ	Dynamic viscosity of water
ρ	Density

Indices

c	At phase interface
d	Data/measurements
e	At melt film outflow boundary
ea	Equivalent area
ec	Equivalent circumference
f	Freezing point (of water)
h	Forward (front) heater
ice	Ice, solid phase
imp	Improved model
L	Liquid phase
lat	Lateral
m	Model/modelled
mh	Melting head
s	Ice screw
sup	Supplementary
tot	Related to the complete probe

speed is lower than the speed of conventional drilling systems, melting probes have three major advantages: (1) Cleaning of melting probes is simpler than cleaning conventional drilling systems, hence it is easier to set up an operation protocol compliant with environmental and planetary protection regulations, (2) melting probes are less service-intense during operations, hence can be used in a (semi-) autonomous mode, and (3) the drill hole must not be kept ice-free, in contrast to deep ice drilling with mechanical drills which typically require contaminating drilling fluids maintain an open drill hole (Talalay, 2014). These aspects are vital for future exploration and, therefore, ice melting probes are considered a key technology of future missions aiming at penetrating the moons' thick icy shells, advance to the global water oceans beneath, analyse their habitability and possibly find traces of life (Konstantinidis et al., 2015; Waldmann and Funke, 2019).

For the preparation of such an ice exploration mission, a detailed understanding of how the probe's input power translates into descent velocity and melting efficiency is mandatory. Given a specific deployment site of interest, such knowledge can be leveraged to predict melting velocity and efficiency of a specific probe design. Equally important, it supports the model-based development of a probe by determining required power and energy demand based on the mission's feasibility constraints, for example, a minimally required descent velocity. We will refer to both cases as 'performance predictions' in the ongoing of this publication.

Performance predictions can either be based on data acquired during past lab experiments and field tests, or on numerical simulation of physical models. An analytical model to estimate the power requirement of a melting probe including lateral conductive heat loss was first developed by Aamot (1967). Later, a parametrized approximation has been proposed by Ulamec et al. (2007). Both were widely used but remained unverified by laboratory or field data. Schüller and Kowalski (2019) assessed via a numerical model convective losses in the vicinity of a melting probe, and used this to quantify the corresponding efficiency as a function of probe surface temperature, contact force and ice temperature. Their model is qualitatively supported by the results of laboratory tests (Talalay et al., 2019), however, relies on the assumption of a melting probe that is laterally isolated. By comparing the aforementioned models with experiments, another study by Li et al. (2020) affirms the importance of the particular melting head design with respect to its shape and heater arrangement. This study also confirmed the principle ability of thermal melting probes to penetrate dirt layers with reduced speed, which was earlier demonstrated in laboratory tests by Kömle et al. (2018). Another numerical study by Li et al. (2021) pronounced the significance of the overall melting head design (including the material, as well as the configuration and kind of heater elements) over simply focusing on the tip shape and angle, building on the findings that the external geometry does not seem to be the determining factor to estimate the efficiency. Aamot's approach was recently enhanced by Durka et al. (2022) to reflect the effects of temperature-dependent ice properties in their model called Aamot^{++}. While this is an important adoption to make the model applicable for a wider range of environments, including icy moons, our results show significant performance deviations in the field from the model prediction even for environments that match the original range of validity. Moreover, the Aamot^{++} model requires information that is hard to estimate or measure in the field, such as the lateral clearance between probe and water–ice interface.

In a well-controlled laboratory environment, do Vale Pereira et al. (2023) investigated the predictability of simple melting probes with cylindrical shape under conditions including a combination of ambient pressure and ice temperature that is comparable to an icy moon environment. Given a particularly good understanding of thermodynamic conditions, especially well known ice properties, they found good agreement between existing models and controlled laboratory experiments. However, the restricted knowledge about the environment in natural terrestrial ice, but even more so in extraterrestrial ice, currently limits the benefit for scientific missions. Scientific payload inside a probe, which is a mandatory element of space exploration missions and polar research, further complicates the modelling of the melting

process, as it implies probe design trade-offs between efficiency and practicability that may be hard to project into models. Nonetheless, a model that describes the melting probe and the physical processes — no matter how sophisticated it is — can only be of high accuracy if the environmental parameters are exactly mapped to the model. The uncertainty inherently introduced by natural ice will always be a limiting factor of the whole modelling approach.

Although active research is in progress on both approaches, numerical modelling and data-driven analyses, each approach alone has yet its weaknesses. A sole data-driven prediction cannot easily be extrapolated to ambient conditions outside the mission's regime, while simulations are often based on strict idealizations and assumptions (which were well summarized by do Vale Pereira et al. (2023)). To remedy these problems, we combined both approaches and thus are working towards a hybridized prediction that is informed both by measured data and our current best knowledge on the physics of the system. The models shown here serve as a starting point for further developments. Their refinement is the subject of ongoing research and will be shown in future publications.

In this paper, we analyse data acquired with a steerable ice-melting probe called 'EnEx-IceMole' (Dachwald et al., 2014) and compare it with numerical modelling results. The original performance-related field test data is shown to have a physical basis with minimal potentially falsifying assumptions. Then, we investigate how well existing thermodynamic models perform with real scientific mission profiles instead of focusing on the most accurate model possible. For this purpose, we also offer an engineering-driven approach to estimate the efficiency of the probes, that can incorporate arbitrary heat loss models and is not limited to those used in our work. Instead, we invite researchers to also use other models with our framework that are best suited for their particular use case.

The EnEx-IceMole is part of the IceMole-family of melting probes developed at FH Aachen University of Applied Sciences, which are particularly characterized by an actively driven ice screw at the melting head and a square-shaped cross-section. The EnEx-IceMole was originally developed as part of the Enceladus Explorer (EnEx) project, where also a concept study for a lander mission to Enceladus was elaborated. This concept includes the deployment of a lander with an ice melting probe in the vicinity of the Tiger stripes at Enceladus' South Polar Region: After landing at a safe spot, the probe melts towards places of liquid water in the plume-feeding crevasse to search for biosignatures, while it actively avoids mission-threatening obstacles (Konstantinidis et al., 2015).

The data used in this study were collected in a field test and a sampling mission in 2014. A field test in June 2014 was used to test the melting probe's systems, before the probe was shipped to Antarctica. In international cooperation with the Minimally Invasive Direct Glacial Exploration (MIDGE) project, the objective of the sampling mission in the Antarctic summer 2014/2015 was to return a clean englacial sample from the subglacial brine reservoir supplying the Blood Falls at the snout of Taylor Glacier (Badgeley et al., 2017).

First, we describe the melting probe in Section 2 and the field test scenarios along with some key insights from the respective logged data in Section 3. Then, we introduce two probe-specific measures of efficiency based on previously published heat loss models and a method to superpose results from both models.. Additionally, we present an improved heat loss model which combines previous approaches by including convective melt film heat loss into the estimation of the lateral conductive heat loss. It serves as the basis of ongoing research. To validate the improved model and the derived efficiencies, we calculate them for both field-test scenarios based on the respective heat loss models and compare the results with the actually achieved performance (Section 4). In the next step, we apply a trajectory model based on the previously introduced heat loss models, which also highlights the impact of deviations between modelled and achieved efficiency for mission design (Section 5). We close the paper with a discussion of our findings (Section 6) and conclusions (Section 7).

2. Ice-melting probe description

2.1. Mechanical design

All field test data reported in this paper were obtained with a probe called 'EnEx-IceMole' (Fig. 1). 'IceMole' is the name for a series of steerable ice-melting probes developed at FH Aachen University of Applied Sciences since 2010 (Dachwald et al., 2014). The 'EnEx-IceMole' was specifically built for the DLR-funded Enceladus Explorer (EnEx) project. The main objective of this project was to develop and test navigation technology for deep ice penetration, as required for the future exploration of the Saturnian moon Enceladus and other icy moons in the outer Solar System (Konstantinidis et al., 2015; Kowalski et al., 2016).

The IceMole is equipped with a forward heating system, which enables ice penetration by melting the ice in the direction of motion, and supplementary heating systems, which are necessary for curve melting and to avoid lateral re-freezing, but do not contribute to ice penetration in longitudinal direction. In case of the IceMole, the supplementary heaters include side-wall heaters to prevent the probe from stalling and backplate heaters to additionally enable retraction. We will use the terminology of forward and supplementary heaters in the context of thermal melt probes beyond this publication to ensure improved comparability of technical data and analyses.

The approximately 60 kg IceMole is made steerable by an ice screw at the tip of its copper melting head and a 2 m long pencil-like shape with a square-shaped 15 cm × 15 cm cross-section to provide the necessary counter-torque for the screw. The 6 cm long ice screw is driven by a 25 W servo-controlled motor and a gear system. Steerability is achieved via differential melting at the melting head, which produces a torque that forces the probe into a curve. Supplementary side-wall heaters support curve-melting. The ice screw leads to a good thermal coupling and hence improved heat transfer into the ice. Furthermore, it allows the probe to melt not only horizontally but also upwards against gravitational pull down as long as the ice screw has a stable contact into the ice. It even allows to penetrate dust and sand layers. To validate the developed probe and navigation technology, the IceMole was used in 2014 for clean drilling into a unique subglacial aquatic environment and extraterrestrial analog at Taylor Glacier (McMurdo Dry Valleys, East Antarctica), known as Blood Falls, with subsequent sample return of englacial brine for chemical and microbiological analysis (Mikucki et al., 2015; Lyons et al., 2019; Campen et al., 2019; German et al., 2021).

2.2. Data acquisition

The standardized log-files generated by the IceMole during melting operation include more than 100 operational parameters, housekeeping information, and error states, which are sent to the base station every 4 s. Occasional packet loss in data transmission resulted in a limited number of increased sampling intervals, which were compensated for by linear interpolation during data post processing.

The data used for our analyses are published separately in a machine-readable format and are freely accessible (Feldmann et al., 2023). It is based on a subset of the raw data comprising timestamps, heater activation patterns and temperatures, distance measurements and ice screw force measurements. We emphasize that this is unadorned data from melt probes that operated in poorly known ice environments. For our analysis, we derived additional measures from the raw data: The penetration distance is provided in the raw data, and is determined based on the ice screw drive step signal (providing the rate of rotation), and the screw's thread pitch. One screw rotation corresponds to 7.5 mm of forward movement and 20,000 motor step commands. The logged distance increments are corrected by detecting motor stall with a Hall sensor on-board in a way that step commands that cause a motor stall do not add a distance increment. The melting speed is then calculated

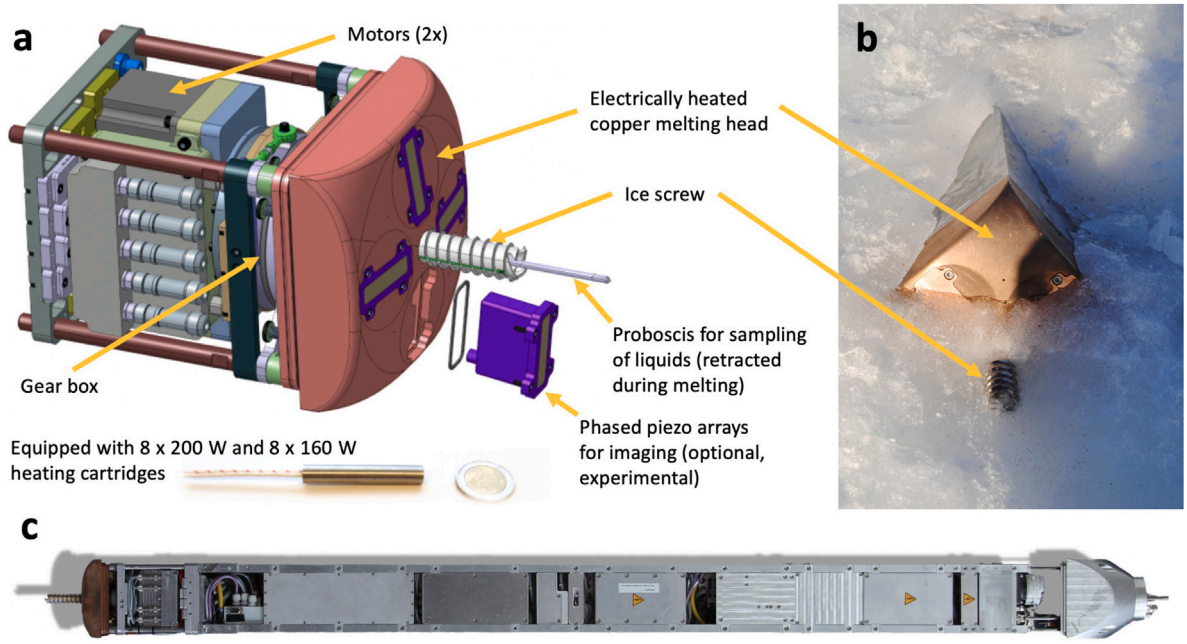

Fig. 1. The EnEx-IceMole: (a) CAD drawing of the melting head. Note that the piezo arrays displayed here were not installed in the two field missions analysed in this work, but were replaced with solid copper dummies for melt performance reasons. (b) Return to the surface of Canada Glacier, Antarctica. The installed copper dummies replacing the piezo arrays are clearly visible here and the evenly shaped ice edge illustrates their good thermal coupling with the surrounding melting head. (c) The full 2 m long probe with the aluminium hull (carrying the side-wall heaters) removed and revealing the payload bays. Credits: FH Aachen UAS.

from the same odometric data, assuming the rate of rotation to be constant over one sampling interval. This approach proofed to be very reliable and robust throughout several probes of the IceMole family.

The contact force is calculated from the probe's buoyancy corrected weight (by reducing the IceMole's mass by the amount of displaced water, which is 45 kg) and the longitudinal screw force, which was measured by two individual sets of strain gauges. We use the mean value of both screw force measurements for our calculations. For non-vertical melting, only the component of the buoyancy corrected weight that points into the direction of movement must be considered in the calculation. The used heating power is calculated from binary states of all heating elements, which can only be either switched on or off. From the raw data bit pattern, the electrical heating power is calculated corresponding to each heater's nominal power. While individual heating cartridges can deviate by up to 5% from their nominal power rating according to the manufacturer, they were selected and integrated into the probe in a way that deviations cancel out to a great extent. This approach ensures that the actual total heat output of the assembled melting head does not deviate by more than 1% from the nominal output. We assigned each heater to one of three groups (melting head, side-wall heaters and back-plate heaters), called heating zones, depending on their respective location. Temperatures are measured separately at each heating element and averaged for each of the three heating zones. In the melting head, the temperature sensors are located at the rear end of each heating cartridge.

Three features must be kept in mind when analysing the housekeeping data: First, the screw drive speed is automatically regulated towards a pre-set contact force and is operated independently from the heater system. Thus, thermal inertia enables forward motion without heating power for a short time, as it also takes place for screw-less probes. Second, all heaters are controlled towards individual temperature set-points using a binary control, but cannot provide fractions of their respective nominal heating power. This behaviour causes discrete steps in the used heating power. Third, instead of the melting head surface temperature T_{mh}, only the temperature inside the melting head T_{h}, near the heating cartridges, could be measured for technical reasons. It is used as the heater controller input, but gives no direct information on the tip surface temperature which is determining the heat flow into the ice.

3. Scenarios and field test data

We present analyses on two different field test settings, which cover two different physical regimes: The Swiss Morteratsch Glacier represents a temperate glacier, meaning ice temperatures are at melting point throughout the year and a channel once melted into the ice remains open. In contrast, the Antarctic Taylor Glacier is classified a polythermal glacier, meaning its ice temperatures are mostly below the melting temperature, but can occasionally reach this temperature at the rock–ice-interface at the bottom of the glacier. As a consequence, a probe requires additional measures to prevent stalling or freezing in on the Taylor Glacier.

The ultimate depths of the drill holes were measured individually and agreed well with the on-board measurement. Both measurements were within a few centimetres, which is in the order of magnitude of the roughness of the ice surface used as the measurement reference. Thus, at least on a mean velocity basis, the screw rotation measurement was validated to be sufficiently precise.

3.1. System test at Morteratsch Glacier, Switzerland

In June 2014, the EnEx-IceMole was deployed several times at Morteratsch Glacier in Switzerland. While the eight-day field-test mainly aimed at optimizing the probe's navigation capabilities, operational parameters and housekeeping data were also logged. In this paper, we use the data from the last deployment of this field test campaign, because it provided the most uniform long-time melting process of all the runs with nearly 4 h of fully submerged melting.

The probe was deployed into the temperate glacier ice at an inclination of about 50° with respect to the horizontal direction. Accordingly, it reached a depth of about 5.3 m after a melting distance of 6.9 m. According to the glacier classification, the ice temperature was assumed to be $T_{\mathrm{ice}} = 0\,^{\circ}\mathrm{C}$ (Harrison, 1972). This assumption is supported by observations on site, where no size reduction was detected for any melt hole and in any depth during the test campaign.

As the operations protocol was tailored towards an investigation of the probe's localization capabilities, the probe was intentionally halted

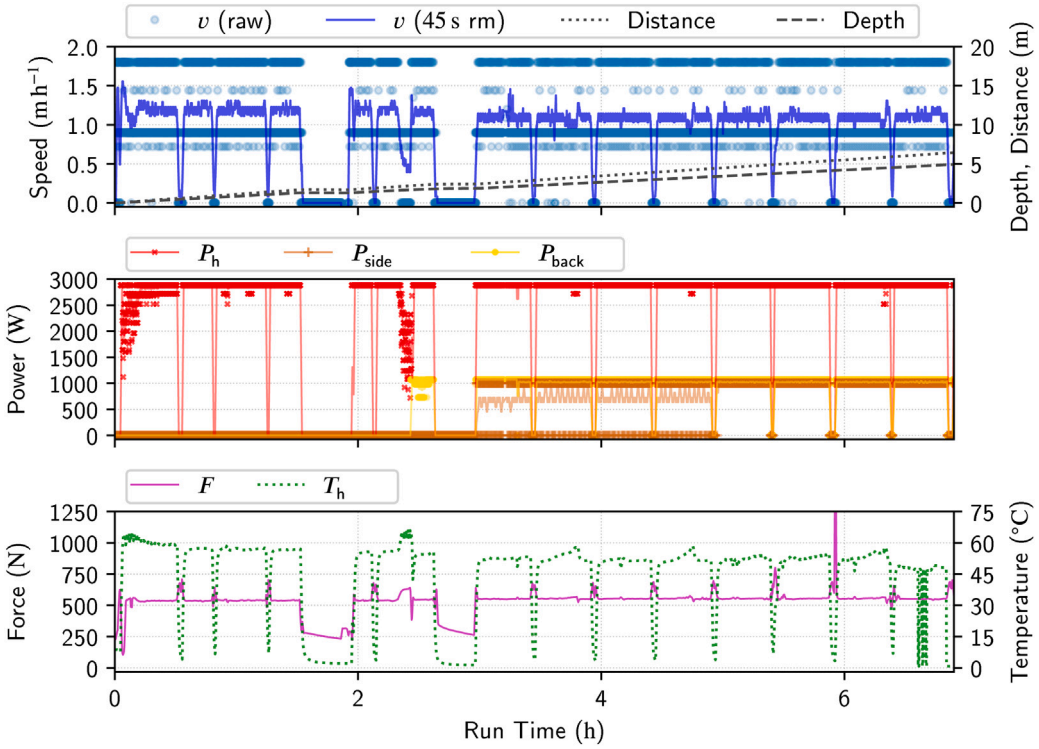

Fig. 2. Logged data from the field test on Morteratsch Glacier. Drops in velocity and heating power are caused by intentional melting stops. The top panel shows the raw velocity data points, which are directly derived from the distance measurement increments. The solid blue line in the top panel shows a rolling mean (rm) over 45 s of this data.

several times for additional acoustic and magnetometer measurements. Consequently, the logged data presented in Fig. 2 shows frequent drops in velocity and heating power, occurring in intervals of about 30 min. Apart from these stops, and once the IceMole was fully submerged into the ice, it demonstrated a very constant melting speed averaging 1.1 m h^{-1}. During the first 2.5 h, the probe proceeded with 1.21 m h^{-1}, which is about 10% faster. The change in speed is linked to a reduction in T_h from 60 to 55 °C which is shown in the bottom panel of Fig. 2.

The odometric distance measurement is derived from the screw-drive step commands, which are corrected by a Hall sensor based stall detection on-board of the probe. As can be seen in the top panel of Fig. 2, preset operating points are commanded by the motor controller that lead to discrete distance increments. Averaging over 45 s yields a better representation of the physics behind the data.

The mid panel in Fig. 2 shows that, after an initial run-up phase, the probe used its full available melting head heater power of 2880 W nearly constantly except for the intentional stops. Supplementary heaters were activated after 2.25 h in the back first and subsequently also along the side walls. Automatic side wall heater activation averaged at two heater activations in three controller steps (leading to an average P_{side} of about 670 W) during the first two hours after activation and at one active heater at a time afterwards (leading to an average P_{side} of about 1000 W). For the back heaters, only the four installed 250 W heating cartridges were active, which leads to a constant P_{back} of about 1000 W after activation.

The bottom panel in Fig. 2 exposes short increases in contact force when the melting head temperature drops after initiation of a measurement stop. The penetration rate was reduced by switching off the heaters only, while the screw drive continues to target a constant contact force. However, the melting head cools down rapidly, so that the probe soon comes to a standstill. The target temperature for the temperature sensors in the melting head was set to 60 °C during the first 2.5 h, and was reduced to 55 °C subsequently.

3.2. Brine sampling mission at Taylor Glacier, Antarctica

In November 2014, the EnEx-IceMole was deployed at Blood Falls above the snout of the Taylor Glacier in Antarctica's Dry Valleys, after having successfully demonstrated its capability to take clean water samples in compliance with the requirements of Antarctic Specially Protected Areas (ASPAs) in the previous year at Canada Glacier. Details of the associated regulations for the Blood Falls area can found in Antarctic Treaty Secretatriat (2018). During 12 days of preparations, there were two preliminary sampling attempts, before the IceMole was eventually launched on its successful sampling mission. Here, we present the data of the second and third (final) attempt.

At Taylor Glacier, an ice temperature of −17 °C was measured about 1 m below the surface, which meets the annual average air temperature at the location (−17.1 °C) and is also consistent with values determined for a depth of about 0.9 m in November 1995 (Hoffman et al., 2008). During one test, the IceMole intentionally froze in at a depth of 18 m, near the brine reservoir. After several hours of cooldown, a steady-state temperature of −7 °C was measured, which is also consistent with previously published measurements of brine temperature (Lyons et al., 2019). As a simplification, we use a linear interpolation between these values to model the local ice temperature versus depth.

In a second attempt on November 22nd, the probe was launched pointing steeply downwards towards the proposed brine location at an angle of about 20° with respect to the vertical direction. Here, the IceMole operated in a dry melt channel first, which then filled with meltwater and later drained again when passing a crack in the ice.

On November 29th, the IceMole was launched from a depth of 3.65 m inside the channel previously melted during the second attempt. It penetrated the glacier at the same angle of about 20° with respect to the gravitational acceleration towards the proposed target area. After a travelled distance of about 17 m, the meltwater samples showed increased electrical conductivity, which is a clear indicator that the probe had reached the brine. A groundwater pump was used to transfer the brine to sample containers at the surface. The probe was successfully recovered about 30 h after its release to the ice.

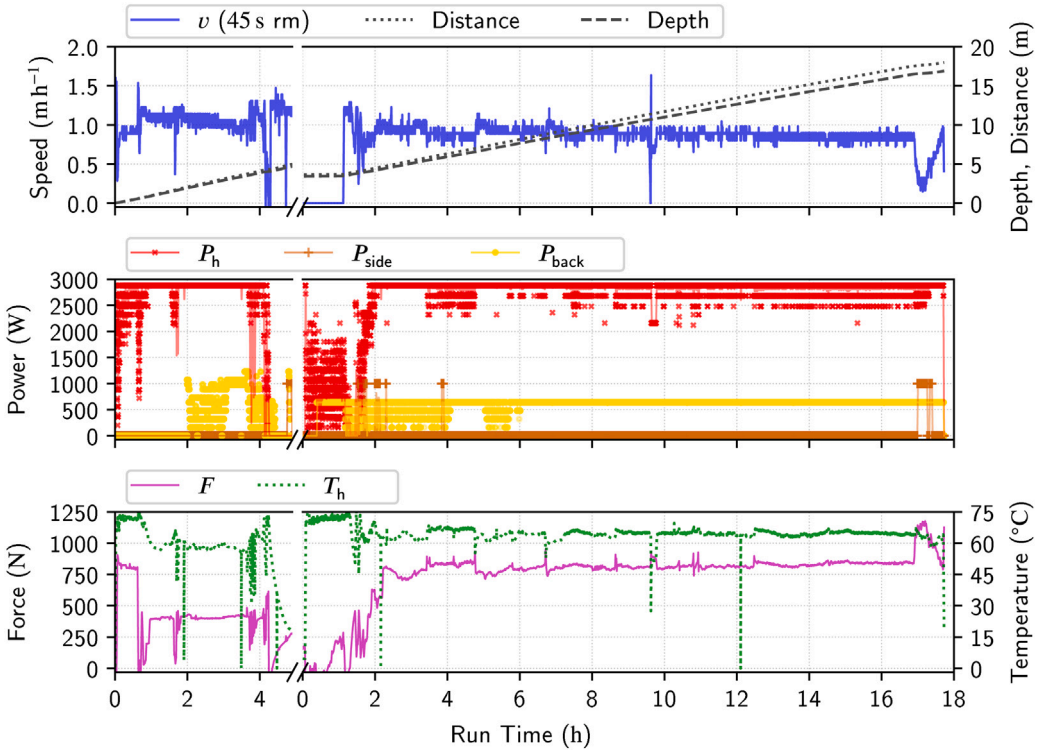

Fig. 3. Logged Data from the final demonstration on the Taylor Glacier. Here, only the smoothed penetration rate is displayed in the top panel to improve readability. The raw data has the same characteristics as shown in Fig. 2 and does not enhance understanding.

The data of this run is presented in Fig. 3. As the probe was launched from the previous melt channel, the figure also includes the data of the previous run on the left side for completeness, although the break between both attempts lasted several days. In between the two melt attempts, minor repairs where carried out on the probe as it was damaged during recovery. Despite the interruption, all technical specifications were preserved for the subsequent operations. However, further analysis concentrates on the data of the third attempt (starting at a depth of 3.65 m) because of the more stable ambient conditions. It is characterized by a 16-hour long phase of almost constant melting speed and steady ice penetration. While descending, the speed decreases to about 90% of its initial value of about $1\,\mathrm{m\,h^{-1}}$, despite the ice temperature increased and the heating power remained mostly constant. Although it was not documented in this case, a reason for the velocity reduction could be the accumulation of dust particulates in front of the melt head: While penetrating not perfectly clean ice, particulates that were trapped in the ice become free and sink towards the bottom of the hole. Accumulating over time, the particulates can reduce a probe's velocity measurable, as it was shown by Kömle et al. (2018). The original (non-averaged) velocity data was omitted in the top panel of Fig. 3 for improved readability and only the averaged data is shown.

The mid panel of Fig. 3 displays that supplementary heating was active during the whole mission to achieve target temperatures of 5 °C along the probe walls and 10 °C at the back heaters. The idea of a reduced heat transfer between melting head and ice by accumulating particulates is supported by the fact that the average melting head heating power slightly decreases within the last 10 h of melting (the frequency of single inactive heating cartridges increases), while T_h remains unchanged.

As can be seen in the bottom panel of Fig. 3, the screw force setpoint was gradually increased during the first two hours of melting and subsequently remains at 750 N until reaching the sub-glacial iron-rich brine. Values of negative contact force (e.g., during the first hour and after reaching the brine) match moments when the melting head did not establish contact with the ice. Consequently, these events also coincide with moments of no melting progress in the velocity plot.

4. Efficiency and performance assessment

Engineers are very interested in realistic predictions for energy demand, required power or achievable melting velocity, both in the design process of a melting probe and during mission planning. Here, we define two efficiency factors helping to estimate the performance of a probe design by exploiting results of the energy balance approach as a lossless reference case. We distinguish the evaluation of only the melting head surroundings, on the one hand, and the analysis of the entire probe vicinity, on the other hand.

In the analysis of power requirements and heat loss, we distinguish heat rates $\dot{Q}$ and heating power P, although both are identical measures from a physical point of view. We use $\dot{Q}$ to express heat rates in physical processes, while P describes the power that was technically provided or is required by the probe to achieve a certain performance.

Furthermore, we incorporate the outcome of a numerical study by Boledi et al. (2023) which aimed at the prediction of the heat transfer between melting head with transient heating power and an ice surface. The results show that for a probe comparable to the EnEx-IceMole, it takes about 45 s since switching on the heaters to reach about 99% of the steady state melt velocity. To account for the probe's changing heater states during melting, we therefore use the non-centred rolling mean with an averaging time of 45 s when working with logged power data. This approach is also validated to be reasonable by comparison with the measured data next to the measurement stops on the Morteratsch Glacier.

4.1. Melting velocity and efficiency in absence of power losses

A common engineering approach to estimate the characteristics of a melting probe is based on a simplified energy balance (Aamot, 1967). It defines the minimum required energy E to melt an ice mass $m_\mathrm{ice} = \rho A s$ when neglecting all sources of heat loss. The ice mass is calculated using the ice density ρ, the probe's cross-sectional area A and the covered distance s. Based on the energy necessary to heat up the ice to its melt

temperature and to perform the phase transition, the required energy is

$$E = \rho A s \left[c_\mathrm{p} \left(T_\mathrm{f} - T_\mathrm{ice}\right) + h\right] , \tag{1}$$

where c_p is the specific heat capacity, h is the latent heat of melting and $T_\mathrm{f} - T_\mathrm{ice}$ is the offset between melting temperature and ice temperature. The minimum required lossless melting head heating power is obtained by time derivation and introducing the melting velocity as $v = \frac{ds}{dt}$, yielding

$$P_\mathrm{lossless} = v A \rho \left[c_\mathrm{p} \left(T_\mathrm{f} - T_\mathrm{ice}\right) + h\right] . \tag{2}$$

Throughout this paper, the melting velocity is also referred to as penetration rate or descent velocity. Eq. (2) can be easily transformed to calculate the achievable velocity v for a specific probe geometry and forward power setting:

$$v = \frac{P_\mathrm{lossless}}{A \rho \left[c_\mathrm{p} \left(T_\mathrm{f} - T_\mathrm{ice}\right) + h\right]} . \tag{3}$$

Please note that Eqs. (1) to (3) assume the material properties of ice to be constant with changing temperatures.

The efficiency of a melting probe can be formulated from a power or velocity point of view. Both yield identical results, as power and velocity are directly related by Eq. (2). In agreement with Ulamec et al. (2007),[1] we call

$$\eta = \frac{P_\mathrm{lossless}}{P_\mathrm{h}} \tag{4}$$

the general melting efficiency. Here, P_h is the actually used heating power in an experiment or field test, or incorporates additional heat loss rates when evaluating simulations. By substituting Eqs. (2) and (3) into Eq. (4), it can also be written using the measured (or, in the case of simulations, the predicted) velocity v, and the theoretical lossless maximum velocity v_lossless (Li et al., 2020):

$$\eta = \frac{v}{v_\mathrm{lossless}} \tag{5}$$

4.2. Efficiency considering power losses

If a melting probe is equipped with supplementary heaters, the power used apart from the melting head should not be considered to contribute to the actual phase change process. Instead, it is only required to prevent the probe from stalling, freezing in or to maneuver the probe (Aamot, 1967). Depending on the point of view of an analysis, it then can be desirable to include supplementary heating power in the efficiency calculation or to concentrate on thermal processes around the tip and inside the melting head only.

When focusing on the processes around the melting head, we define

$$\eta_\mathrm{mh} = \frac{P_\mathrm{lossless}}{P_\mathrm{lossless} + \sum P_\mathrm{loss,\ mh}} , \tag{6}$$

which includes the heat losses occurring between the heat source inside the probe (e.g., heating foils or cartridge heaters) and the phase change interface. P_lossless is the required melting head heating power under lossless conditions (according to Eq. (2)) when targeting a specific penetration rate. When analysing field-test or experimental data, the full denominator term equals the logged forward (typically: melting head) heating power. The sum of heat loss rates may comprise heat loss by thermal conduction towards rear structural parts or into unintentional heat sinks (like parts of the payload). Also, losses due to the heat conduction between heat sources and the melting head surface being limited by material properties may impact the melting head efficiency. Furthermore, the melt process generates a constant mass flow of warmed liquid water around the tip, which is responsible for convective heat loss between probe and phase interface.

For a stationary melting process, internal conductive heat losses can be assessed by numerically solving the heat equation for a given geometry using the finite element method. Though, for complex geometries, this method is computationally intensive. Convective heat loss inside the melt film can be estimated according to Section 4.3, following the approach of Schüller and Kowalski.

To examine the performance of the entire probe operating in a specific environment, the total energy budget along its length must be considered. If applicable, this can also include power transmission from the surface. Therefore, η_tot must be formulated for a control volume around the full probe, yielding

$$\eta_\mathrm{tot} = \frac{P_\mathrm{lossless}}{P_\mathrm{lossless} + \sum P_\mathrm{loss}} . \tag{7}$$

In this case, all quantifiable models should be covered by the sum of losses, including the aforementioned heat loss occurring at the melting head. When evaluating field-test or experiment data, the total power provided to the probe can also contain the power draw by housekeeping systems or additional drive systems (e.g., ice screw motor). However, the heating power is typically about two orders of magnitude greater and is thus the determining factor.

Note that due to the interaction between superposing sources of heat loss, the heat losses that were included in η_mh before may be subject to recalculation now, as we describe in Section 4.6.

The power required by payloads must not be included in the total power, though, as it does not contribute to the melting characteristics of the probe as a carrier vehicle. Nevertheless, a payload can be determinant for the overall design and dimensions of a probe and thus can influence its efficiency as a side effect.

Again, all components of P_loss may be translated into velocities with Eq. (3). The result of each loss fraction can then be interpreted as a velocity penalty Δv resulting from heating power not being used for ice penetration. Subtracting all Δv from the lossless v_lossless eventually yields velocity-based η_mh and η_tot analogue to Eq. (5) as

$$\eta = \frac{v}{v_\mathrm{lossless} - \sum \Delta v} , \tag{8}$$

where v_lossless is the achievable velocity for a given heating power under lossless conditions according to Eq. (3).

4.3. Heat losses due to convective processes in the melt film

During melting, a thin liquid film establishes between ice surface and melting head. The liquid melt film is radially squeezed to the side by the contact force that the probe exerts on the film. Schüller and Kowalski (2019) derived a method to estimate the heat rate $\dot{Q}_\mathrm{e}$ that is lost by convecting melt water and does not contribute to melting in front of the probe. We denote by $\dot{Q}_\mathrm{e}$ the convective heat loss rate. Note however, that here *loss* refers to the fact that the corresponding power does not contribute to forward motion of the melting probe. A holistic melting probe model may as well take into account that the heated melt water can be utilized to counteract refreezing while flowing past the probe, thereby lowering the need for additional side wall heaters. Consequently, $\dot{Q}_\mathrm{e}$ must not necessarily be added to other sources of heat loss without careful review (also see Section 4.6).

The two-dimensional model by Schüller and Kowalski (2019) relies on a generalized lubrication approximation in the melt film coupled to a Stefan type problem to account for the melting of the ice. Boundary conditions at the melt head surface are given as no-slip, zero inflow and a given heat flow rate $\dot{Q}_\mathrm{mh}$. Note, that in general $\dot{Q}_\mathrm{mh}$ might deviate from the heat flow rate at the heaters $\dot{Q}_\mathrm{h}$, due to realistic thermal conductivity values and a non-perfect insulation. Boundary conditions at the phase interface are given by no-slip, a mass inflow that balances the melted ice due to forward motion and a heat flux jump referred to as the Stefan condition. The radial outflow is bounded by the hydrostatic

[1] In Ulamec et al. (2007), η is mistakenly defined as $\frac{P_\mathrm{h}}{P}$ instead of $\frac{P}{P_\mathrm{h}}$, but their results correspond to the latter definition and remain valid.

pressure inside the melt channel in the depth of the melting head. The physical properties of ice and water are assumed to be independent of temperature changes.

Schüller and Kowalski (2019) derived the efficiency η_{conv} that quantifies the effective heat flow rate into the ice $\dot{Q}_{\mathrm{c}}$ as

$$\dot{Q}_{\mathrm{c}} = \eta_{\mathrm{conv}} \cdot \dot{Q}_{\mathrm{mh}} \tag{9}$$

with

$$\eta_{\mathrm{conv}} = \frac{1 - \frac{3}{20\alpha_{\mathrm{L}}} \left(\frac{\rho_{\mathrm{ice}}}{\rho_{\mathrm{L}}} \upsilon R \right)^{4/3} \left(\frac{3\pi\mu}{2F^*(g)} \right)^{1/3}}{\frac{7}{20\alpha_{\mathrm{L}}} \left(\frac{\rho_{\mathrm{ice}}}{\rho_{\mathrm{L}}} \upsilon R \right)^{4/3} \left(\frac{3\pi\mu}{2F^*(g)} \right)^{1/3} + 1}, \tag{10}$$

using the density ratio of frozen and liquid water $\frac{\rho_{\mathrm{ice}}}{\rho_{\mathrm{L}}}$ and the dynamic viscosity of liquid water μ. The efficiency also depends on the radius of the probe with circular-cross section R. A simple approach for non-circular cross-sections is provided in Section 4.5. The buoyancy corrected contact force $F^*(g)$ may be corrected for an additional artificially applied force, for instance generated by a driven ice screw:

$$F^*(g) = F(g) + F_{\mathrm{s}} - \pi R^2 \rho_{\mathrm{L}} g L\,. \tag{11}$$

All in all, the convective heat flow rate $\dot{Q}_{\mathrm{e}}$ that is transported as warm water past the body of the probe is determined to be

$$\dot{Q}_{\mathrm{e}} = \left(1 - \eta_{\mathrm{conv}}\right) \dot{Q}_{\mathrm{h}}\,. \tag{12}$$

More recently, a numerical three-dimensional model also compared different tip shapes with circular cross-sections, namely cylindrical, conical, spherical and paraboloidal tips (Li et al., 2021). However, the comparison with Schüller and Kowalski (2019) using a reference case revealed only negligible discrepancies in melting speed, melting efficiency, and melting head temperature at the same power input. Also, the influence of the tip shape was to be found small and thus not being a driving factor in melting probe design. Tip shapes with a non-circular cross-section were not studied in that work, though.

4.4. Heat losses due to lateral heat conduction into the ice

Ice melting probes usually carry a payload or cable storage in elongated containers behind the melting head to preserve a small cross-sectional area and therefore a lower forward power requirement. However, a probe of elongated shape risks to get stuck in the melt channel, especially when the channel steadily refreezes as in cold glacier ice or in any extraterrestrial setting. This happens because melt water refreezes over time due to conductive heat transfer into the surrounding ice, given the far field ice temperature is below the freezing point of water. Engineering typically addresses this issue by installing supplementary side wall heaters along the probe or by increasing the melting head heating power well above P_{min}.

Aamot (1967) provided a method to assess the lateral heat loss rate for a probe to prevent freezing in based on an approach from Carslaw and Jaeger (1959). He estimates the lateral conductive heat flux at the wall of a volume internally bounded by a circular cylinder. More explicitly, the internal (empty) cylinder represents the melt channel, which is surrounded by an infinite ice volume of initially constant temperature T_{ice}. For a probe of length L and radius R (for non-circular probes, refer to Section 4.5), the lateral heat flux along the probe can be integrated over the probe length, yielding the lateral heat loss rate $\dot{Q}_{\mathrm{lat}}$. With respect to the thermal conductivity λ and introducing the thermal diffusivity $\alpha = \frac{\lambda}{\rho c_{\mathrm{p}}}$, the lateral heat loss rate is given by

$$\dot{Q}_{\mathrm{lat}} = \frac{4\lambda(T_{\mathrm{w}} - T_{\mathrm{ice}})}{R\pi^2} (2\pi R) \int_0^L \int_0^\infty \frac{\exp(-\alpha u^2 t)}{u \left[J_0^2(Ru) + Y_0^2(Ru) \right]} \,\mathrm{d}u\,\mathrm{d}s\,, \tag{13}$$

where J_0 and Y_0 are Bessel functions of the first and second kind, respectively. Further, $T_{\mathrm{w}} - T_{\mathrm{ice}}$ is the temperature difference between the inner cylinder boundary surface and ambient ice at infinite radial distance. At the cylinder wall, which in fact is also the phase change interface, T_{w} would naturally represent the melt temperature of ice. Consequently, $T_{\mathrm{w}} = T_{\mathrm{f}}$ is commonly used as a simple approximation. However, melt channels are slightly oversized in reality, leaving a gap between probe walls and lateral ice surface, which is filled with liquid water when operating in a pressurized environment. In a low-pressure regime on an icy moon, an open melt channel would be filled with vapour. In porous or cracked ice, the melt water can flow away into the surrounding ice, leaving the melting channel mostly dry.

A convenient approximated solution for Eq. (13) is given in Ulamec et al. (2007) as

$$\frac{\dot{Q}_{\mathrm{lat}}}{\upsilon R^2 (T_{\mathrm{w}} - T_{\mathrm{ice}})} = n \left(\frac{L}{\upsilon R^2} \right)^b . \tag{14}$$

Using the fit constants $n = 932\,\mathrm{W\,s\,K^{-1}\,m^{-3}}$ and $b = 0.726$, the approximation is valid for values of $L/(\upsilon R^2)$ in the range of 5×10^4 to $1 \times 10^8\,\mathrm{s\,m^{-2}}$. Note that $\dot{Q}_{\mathrm{lat}}$ scales linearly with T_{w}. In contrast to L, R and υ, which are often pre-determined by the probe design, available power, and efficiency, T_{w} remains as an independent lever for reducing heat loss during operation. In Section 4.6, we present a first attempt to enhance understanding of the effective T_{w} along a probe in order to improve the presented model on lateral heat loss. Both, Aamot's original model and the approximation in (14) assume constant ice properties. A simplified temperature correction is available for the approximation in Ulamec et al. (2007) and described in their publication, though.

To prevent the probe from stalling and freezing in, the ice surface temperature must not fall below the freezing point of water, as otherwise the melt channel would refreeze. The required supplementary heat is typically provided along the side walls of the probe by using side wall heaters. Alternatively, excess heat transported from the tip to the rear by warm meltwater may compensate for additional lateral heating entirely (see Section 4.6).

4.5. Equivalent radius of non-circular probes

Both loss models described above imply melting probes with a cylindrical cross-section. In contrast to this, all probes of the IceMole family require rotational compensation of the ice screw torque and therefore rely on a square-shaped cross-section. In order to still be able to apply the models, we introduce an equivalent radius derived from the actual probe geometry. While this is a valid first-order correction in terms of energy balance, one has to be aware that the equivalent radius does not account for the correct physical mass and momentum processes and can thus differ depending on the model.

Aamot's model described in Section 4.4 evaluates the heat loss through a cylinder surface, which is based on local values of the circumference integrated over the probe length. Consequently, we use the radius of an equivalent circular circumference as an approximation to calculate the lateral heat loss. Based on the circumference of a square $C_{\square} = 4a$ and that of a circle $C_{\circ} = 2\pi R$, the radius of a circle with equivalent circumference R_{ec} calculates to

$$R_{\mathrm{ec}} = \frac{2}{\pi} a\,, \tag{15}$$

where a describes the square's edge length.

Whereas in the approach by Schüller and Kowalski (2019), the convective losses are evaluated based on the heat flux through a circular area. Hence in this case, the radius of a circle with an equivalent area R_{ea} must be chosen. With the area of a square $A_{\square} = a^2$ and that of a circle $A_{\circ} = \pi R^2$, it, correspondingly, calculates to

$$R_{\mathrm{ea}} = \frac{1}{\sqrt{\pi}} a\,. \tag{16}$$

Equivalent radii for geometries other than squares can be derived accordingly.

4.6. Superposition of heat losses in the melt film and due to conduction into the ice

While the two presented models cover some major sources of heat loss during melting, both are not mutually exclusive and a simple addition of their respective results would not lead to a correct view on the heat budget. Rather, one must assume that $\dot{Q}_e$ is available as additional heat input along the probe's length, because warm water is displaced in front of the probe and flows towards the rear. Therefore, $\dot{Q}_e$ contributes to the lateral heating requirement and reduces the additional heating power required by supplementary heaters. This concept is also supported by Schüller and Kowalski (2019), who provide a method for determining the maximum possible probe length without side wall heaters, calling it the critical refreezing length L^*. It is derived by assuming $\dot{Q}_{lat}(L)$ (Eq. (14)) and $\dot{Q}_e$ (Eq. (12)) to be equal for a certain length L^*, which is then obtained by solving for L.

Nevertheless, an increased water temperature near the probe's front end, in the gap between probe and lateral ice interface, also increases the lateral heat loss locally: As we explained in Section 4.4, the lateral heat loss scales linearly with an increasing wall temperature T_w. By extending the approach from Eq. (13) from the lateral ice interface into the melt channel, we can estimate the increase of the lateral heat loss caused by warm water of the melt film at the melting head being displaced to the rear. In a first and straight-forward implementation and using the nomenclature defined in Fig. 4, the following simplification and assumptions apply:

- Only conductive heat transfer occur in the liquid- or gas-filled melt channel.
- Thermal properties (i.e., thermal conductivity λ and thermal diffusivity $\alpha = \lambda/(\rho c_p)$) of the medium in the melt channel are identical to those of ice.
- The displaced melt film water has the same temperature as the melting head surface (T_{mh}).
- The water temperature decreases linearly along the probe until $l = L^*$, where, according to the definition of L^*, it reaches the freezing point of water. For $l > L^*$, we assume $T_w = T_f$. In our calculations, we use a constant average temperature $T_m = T_f + (T_{mh} - T_f)/2$ for $0 < l < L^*$, but the model is capable of implementing more precise temperature curves that better reflect a probe's transient condition during a melting process.
- When using this model, the melt film heat loss rate is smaller than the lateral conductive heat loss rate (meaning $L^* < L$), because otherwise the probe is not at risk of freezing in at all.
- The side wall temperature of a probe is controlled to be very close to T_f along the full probe length, leading to a narrow and uniform melt cavity around the probe.
- A non-uniform temperature profile with sections of $T(l) > T_f$ along the probe (as it is drawn in Fig. 4) reduces L^* due to the fact that lateral losses increase with the wall temperature T_w in Eq. (13). This feedback effect, which requires iterative calculation, is ignored here.

A more accurate result for $\dot{Q}_{lat}$ is then calculated by evaluating Eq. (13) segment-wise for $0 < l < L^*$ with $T_w = T_m$ and for $L^* \leq l < L$ with $T_w = T_f$, yielding

$$\dot{Q}_{lat} = \dot{Q}_{lat}(T_w = T_m)\big|_0^{L^*} + \dot{Q}_{lat}(T_w = T_f)\big|_{L^*}^{L} . \tag{17}$$

In the case of $L^* \geq L$ (which per definition means $\dot{Q}_{lat} < \dot{Q}_e$), no additional lateral heating is required, and consequently, no meaningful results are obtained by Eq. (17).

The probe analysed here violates at least some of the assumptions listed above: It must be assumed that given the high primary heater temperatures observed in the two field tests (45 to 60 °C), a considerable amount of heat is transferred from the melt water into the ice surround the melting head, leading to a lower T_m than anticipated in our calculations. Further, side wall temperatures and lateral melt film temperatures could not be measured in the field tests and probably vary along the length probe, because the side wall heaters are segmented into only two heater segments per side with a length of approximately 1 m each. Taking the mission at Taylor Glacier as an example, L^* was in the range of 25 to 40 cm most of the time, but the side wall heaters can just be either switched on or off on their full length of 1 m, leading to an uneven melt film temperature even behind $l > L^*$. Nevertheless, the melt channel of the IceMole was observed to be only slightly oversized (about 1 cm wider than the probe).

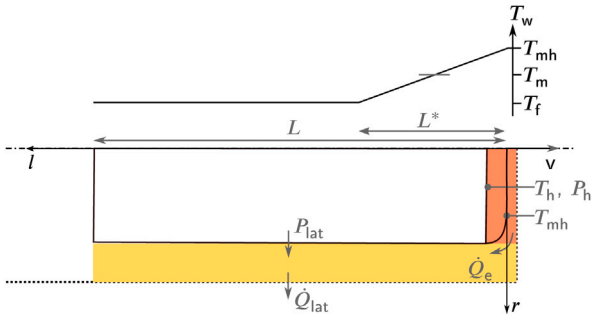

Fig. 4. Heat loss definitions and assumed temperature profile along the probe for the superposition of convective melt film heat loss and lateral conductive heat loss. The melt channel water temperature is assumed to equal the melting head surface temperature T_{mh}, which must be distinguished from heater temperature T_h. The water temperature then decreases linearly until it reaches T_f at length L^*. In the model, a constant average temperature T_m is used for $0 < s < L^*$. Eq. (18) is explained by the heat flow rates into and out the yellow control area, while the orange area marks what is included in η_{mh}. Both the orange and yellow areas are included in the assessment of η_{tot}. (For interpretation of the references to colour in this figure legend, the reader is referred to the web version of this article.)

The heat loss P_{lat} at the probe walls results from the difference of the lateral heat loss rate $\dot{Q}_{lat}$ and the convective heat loss rate at the melting head $\dot{Q}_e$, as it is accounted for the yellow area in Fig. 4. A negative result for P_{lat} origins in $\dot{Q}_{lat} < \dot{Q}_e$ and $L < L^*$. Only in this case, the absolute value of the result must be considered ultimately lost when calculating η_{tot}. These presumptions lead to the lateral heat loss at the probe's side walls

$$P_{lat} = \begin{cases} \dot{Q}_{lat} - \dot{Q}_e & \text{if } \dot{Q}_{lat} > \dot{Q}_e \\ 0 & \text{if } \dot{Q}_{lat} \leq \dot{Q}_e \end{cases} , \tag{18}$$

where in the second case the convective losses at the melting head make up for the total lateral heat loss.

The two selected scenarios from Section 3 demonstrate both cases of Eq. (18). In warm ice close to or at the temperature of fusion (such as on temperate glaciers like Morteratsch), $\dot{Q}_{lat}$ becomes very small or zero. In this case, supplementary heaters are often expendable for straight melting, as can be seen from Fig. 5a: The convective heat loss $\dot{Q}_e$ easily reaches 5 to 8% of the used heating power P_h, even when using an ice screw to increase the contact force artificially. Consequently, the lateral heat loss is completely compensated by $\dot{Q}_e$ and no additional lateral heating power is required. Thus, supplementary heating was unnecessary in this case, even in a case where the temperate glacier would have been slightly colder than 0 °C near the ice surface due to seasonal fluctuations.

Modelling P_{lat} for the Blood Falls scenario (as shown in Fig. 5b) indicates a decreasing lateral heat loss with increasing depth and ice temperature, whereas the convective losses remain around the same level of $\dot{Q}_e = 110$ W (or about 4% of P_h). The plot illustrates the first case of Eq. (18), where $\dot{Q}_e$ reduces the required P_{lat} to compensate $\dot{Q}_{lat}$. The decreasing spread between $\dot{Q}_{lat}$ and $\dot{Q}_e$ also causes an increase in the critical refreezing length. By advancing into warmer ice, it increased from about 0.25 to 0.4 m, which is still not sufficient for the 2-metre long EnEx-IceMole, though. Consequently, supplementary

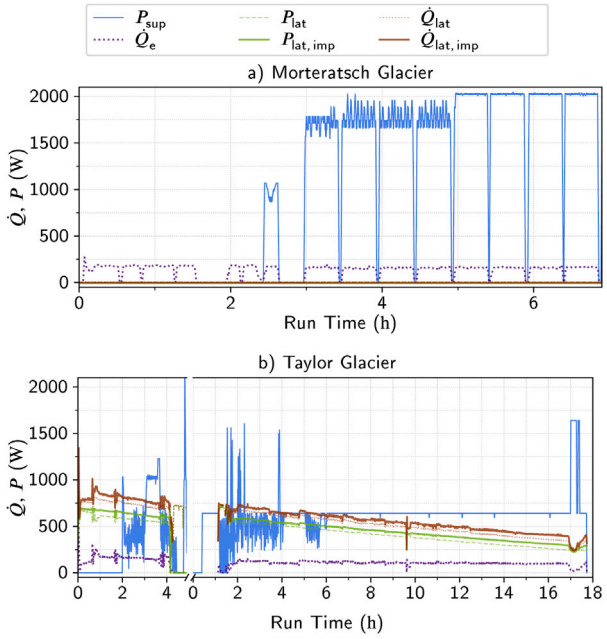

Fig. 5. Comparison between the used supplementary heater power P_{sup} and the heat loss according to Eqs. (14), (17) and (12), as well as the resulting lateral heat loss at the probe's side walls P_{lat}. Melting through the warm ice of Morteratsch Glacier does not require supplementary heating power at all, as $\dot{Q}_{lat}$ remains zero. Yet, convective heat loss of about 200 W occurs at the melt head. Whereas in the colder Taylor Glacier, the occurring $\dot{Q}_e$ partly compensates for $\dot{Q}_{lat}$, consequently reducing P_{lat} compared to $\dot{Q}_{lat}$. The improved lateral heat loss model yields about 8.6% higher results for $\dot{Q}_{lat}$ and P_{lat} in the Taylor Glacier scenario. In absolute numbers this means an increase of ca. 40 W. In both cases, a significant amount of supplementary heating power was used unnecessarily, with the spread between P_{lat} and P_{sup} becoming extreme on the Morteratsch glacier.

heaters were used in this run with intermittent activity during the first 2.5 h and operated constantly afterwards.

Fig. 5b also demonstrates the model differences introduced by our new model (Eq. (17)). By respecting the increased melt water temperature in the melt channel, both, the lateral heat loss rate and the required lateral heating power increase by an average value of 8.6%. In warm ice, on the contrary, the same results are obtained by both models, namely no lateral heat loss occurs.

4.7. Achieved efficiency

The application of the aforementioned models gives an impression on their accuracy regarding the predicted heat loss and melting efficiency at different ice temperatures. The efficiency of the melting head and of the entire probe are calculated based on both, the actually used heating power, and the respective loss models. In case of the melting head, we calculate $\eta_{mh,\,data}$ based on Eq. (4) using $P_{lossless}$ from Eq. (2) according to the measured velocity and ice parameters, and the heating power P_h that was actually provided by the melting head heaters (see Fig. 4). The latter is determined by mapping effects of a transient power curve using the non-centred rolling mean of the past 45 s. Because convective heat loss in the melt water layer is the only source of heat loss considered here, $\eta_{mh,\,model}$ is equal to η_{conv} from Eq. (10) in this case. It depends on the measured velocity and contact force, as well as local ice parameters.

We neglect the potential effect of non-vertical melting, which is not covered by the applied models, but could cause a lateral velocity component in theory. The effect is considered very small due to two reasons, namely the low contact force per area (about 2.7% of the one of the melting head when ignoring the ice screw force) and the low areal heating power density (about 5.2% of the one of the melting head) in combination with lower surface temperatures. Both are driving factors in the overall melt performance, as we showed in the previous sections of this chapter and would result in lateral motion that is two orders of magnitude smaller than in forward direction. The leverage effect of the ice screw additionally increases the contact force at the melting head and, at the same time, relieves weight from the down-facing side of the probe. Accordingly, no direct contact between the lower sidewall was recognized as long as it could be observed in the initial melting phases.

Fig. 6 compares $\eta_{mh,\,data}$ with $\eta_{mh,\,model}$, which is based on the same $P_{lossless}$ but takes into account the convective heat losses $\dot{Q}_e$ according to Eq. (12). The plots show that η_{mh} is consistently overestimated by the model. During phases of quasi-stationary melting, $\eta_{mh,\,model}$ exceeds $\eta_{mh,\,data}$ by about 27% in temperate ice and by about 33 to 61% (deviation increases with time, and also with depth and ice temperature) at Taylor Glacier. The distinctive spikes in Fig. 6a mark moments when a melt stop was initiated ($\eta_{mh} \to \infty$, because $P_h = 0$ while $v > 0$) or melting was resumed after a stop ($\eta_{mh} \to 0$, because $P_h > 0$ while $v \approx 0$).

The measured and modelled efficiency with respect to the full melting probe is plotted in Fig. 7. Here, $\eta_{tot,\,data}$ is calculated from (4) using $P_{lossless}$ from (2) according to the measured velocity and ice parameters again, but with the total probe power used for both, the forward and supplementary heaters. The modelled efficiency is calculated with (7). For $\eta_{tot,\,model}$, $\sum P_{loss}$ translates into P_{lat} (Eq. (18)) with $\dot{Q}_{lat}$ according to Eq. (14), while $\eta_{tot,\,model\,imp.}$ relies on the improved $\dot{Q}_{lat}$ from Eq. (17).

In the Morteratsch scenario, modelled and data-based results are mostly constant over time (again, except for spikes during melt stops) after the probe was fully submerged into the ice: Results show a 10% variation over four hours in $\eta_{tot,\,data}$. However, in the Blood Falls scenario $\eta_{tot,\,data}$ exhibits larger variations and the spread to $\eta_{tot,\,model}$ again increases over the run time. This is mainly because the lateral losses are expected to decline in warmer ice of greater depths, but the used supplementary heater power was mostly constant. As a consequence, the predicted efficiency is nearly twice the measured one during the final stage of the run. In the warmer Morteratsch ice, the deviation is even larger, presumably due to excessive and unnecessary usage of secondary heaters. When calculating $\eta_{tot,\,model}$ using the improved lateral heat loss model, the predicted overall efficiency drops by about 1.5 percentagepoints in the Taylor Glacier scenario, slightly reducing the deviation from the observed efficiency. There is no change in results on the temperate Morteratsch Glacier, because lateral heat loss is expected to be zero independent from the used heat loss model.

5. Trajectory model and simulation

The convective efficiency η_{conv} defined in Eq. (10) can also be used to assess the effective local melting speed v_{eff} as

$$v_{eff} = \eta_{conv}\, v_{lossless}. \tag{19}$$

This equation gives then the ice melting probes' melting velocity v_{eff} for a specific set of parameters that describe an ambient icy environment. Following Boxberg et al. (2023), this velocity can be integrated to calculate a global trajectory according to

$$z(t) = \int_0^t v_{eff}\left(P(\tau), T_{ice}(z(\tau)), \ldots\right) \mathrm{d}\tau, \tag{23}$$

where the explicit time dependence of the input power $P = P(\tau)$ accounts for the active control of the probe. The other parameters that describe the icy environment like the ice temperature $T_{ice}(z(\tau))$ depend on the melting probe's location which of course is time-dependent itself.

To compare the calculated trajectory with the IceMole housekeeping information, some assumptions on the ice properties are necessary. These are listed in Table 1. No temperature data for the Morteratsch Glacier was taken during the field test. Since it is a temperate glacier,

Table 1
Summary of physical properties for the simulation.

Property	Unit	Value/Expression	
ρ_{ice}	kg m^{-3}	$933.31 + 0.037\,978T - 3.6274 \times 10^{-4}T^2$[a]	(20)
ρ_{L}	kg m^{-3}	999.84[b]	
μ	Pa s	$1.4147 \times 10^{-4}\left(\frac{T}{226.8} - 1\right)^{-1.5914}$[a]	(21)
g	m s^{-2}	9.806 65[c]	
h	J kg^{-1}	333 430[d]	
T_{f}	K	273.152 519[d]	
$c_{\text{p, ice}}$	J kg^{-1} K^{-1}	$\frac{\left(\frac{T}{273.16}\right)^3\left(1.843 \times 10^5 + 1.6357 \times 10^8\left(\frac{T}{273.16}\right)^2 + 3.5519 \times 10^9\left(\frac{T}{273.16}\right)^6\right)}{1 + 1.667 \times 10^2\left(\frac{T}{273.16}\right)^2 + 6.465 \times 10^4\left(\frac{T}{273.16}\right)^4 + 1.6935 \times 10^6\left(\frac{T}{273.16}\right)^8}$[a]	(22)
$c_{\text{p, L}}$	J kg^{-1} K^{-1}	4219.4[b]	
λ	W m^{-1} K^{-1}	0.555 67[b]	

[a] Ulamec et al. (2007).
[b] Haynes et al. (2017).
[c] Taylor and Thompson (2008).
[d] Feistel and Wagner (2006).

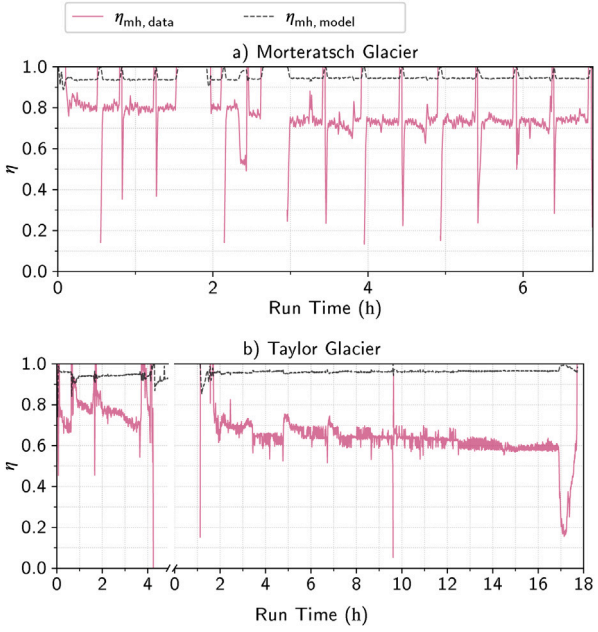

Fig. 6. Achieved and expected melting efficiency according to Eq. (6), considering convective heat loss occurring around the melt head. In (a), except for the spikes indicating melt stops, the uniform characteristics of heating power, contact force and melt head temperature (see Fig. 2) reflect in nearly constant results for $\eta_{\text{mh, m}}$. Nevertheless, the model clearly overestimates the achieved efficiency, showing a constant offset of about 27% after reaching a depth $d = L$. In (b), the deviation between data and model is even larger and slightly increases with increasing melt depth and increasing ice temperature, respectively.

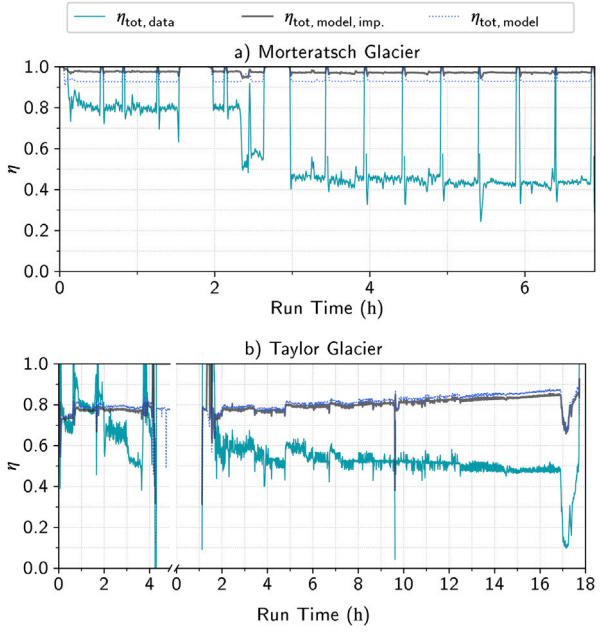

Fig. 7. Achieved and expected melting efficiency according to Eq. (7), considering heat loss around the whole probe. A distinctive drop in efficiency marks the moment where supplementary heating power was activated on the Morteratsch Glacier, resulting in a lower melt efficiency despite a higher ice temperature compared to the Taylor Glacier results. Results from the improved model for lateral heat loss are 1 to 2% closer to the observed efficiency in (b). In (a), results for the traditional and the improved model are identical due to the general absence of lateral heat loss in temperate ice.

we assume the temperature to be 0 °C. For the antarctic field test, we use the temperature information near the surface and at −18 m as described in Section 3. Hence, we approximate the temperature in the upper few metres at Blood Falls with a linear gradient as $T(z) = 256.15\,\text{K} - 0.556\,\text{K m}^{-1} z$.

Fig. 8 shows the simulated trajectory based on the logged information on the field test on Morteratsch Glacier, Switzerland. We use the logged electrical power P_{h} and assumed it is fully converted to the heat flow rate $\dot{Q}_{\text{mh}}$ at the melting probe's head as input for the trajectory model (Eq. (23)). The trajectory model is evaluated with a 100 s time step, while we average the input power over the whole time step. Therefore, the plotted modelled velocity shows smoother changes than the original data sampled every 4 s.

Clearly visible as a prominent feature in the plots are the stops for the navigation system tests at certain depths, where the melting power was switched off. In the centre panel of Fig. 8, it seems that the power is not switched off completely at certain measurement stops, but this is due to the smoothing caused by the averaging over 100 s intervals and the duration of these measurement stops was less than 192 s. Furthermore, the measured melting velocity during the measurement stops is non-zero. This is because the melting head is still hot and not instantly cooled down after switching off the power. In contrast, the model assumes instantaneous response to a change in power. Despite these stops, the modelled velocity is almost constant at 1.30 m h^{-1}. Hence, this can be considered as a steady state melting velocity. The measured melting velocity (excluding the measurement stops) is about 1.2 m h^{-1} at the beginning and slightly decreasing with run time to about 1.1 m h^{-1}. The used power was kept constant, but the contact force actually increased with time from about 530 N to 550 N. This increase in contact force is marginal and does not contribute significantly to a rise in melting speed, since we are already in a domain, where the effect of contact force on melting velocity is very low (Dachwald et al.,

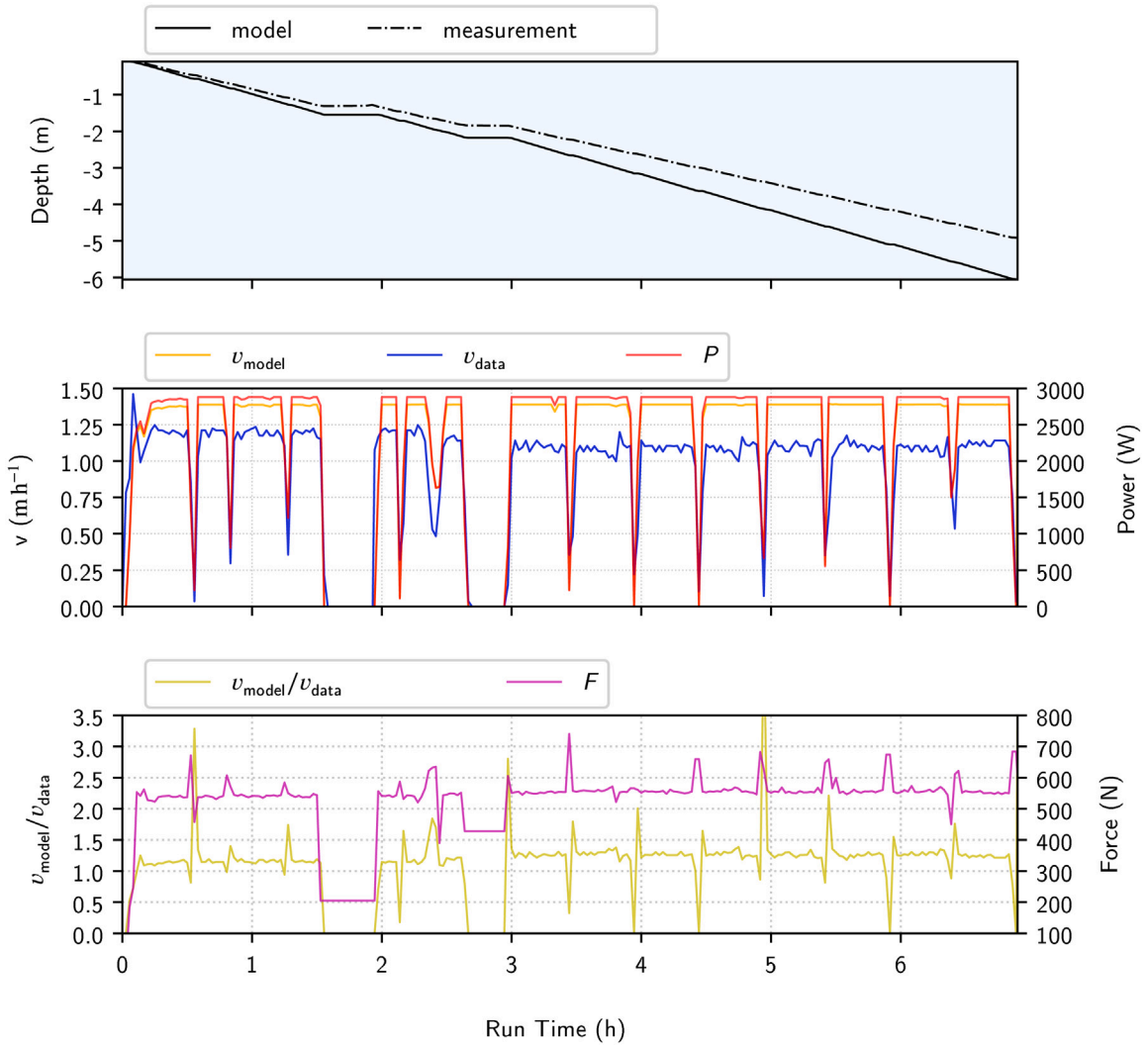

Fig. 8. Trajectory model of field test on Morteratsch Glacier, Switzerland. The top panel shows the trajectory, i.e. the depth location of the probe as a function of the time both from the logs and from the model, while the assumed temperature distribution (here: 0 °C, constant) is plotted in the background. The centre panel shows the electrical power as well as both the modelled and measured velocity of the melting probe. The bottom panel shows the ratio of modelled to measured velocity of the melting probe.

2023). The modelled velocity, hence, actually overestimates the mean measured velocity by about 10% at the beginning and about 20% after 3 h (compare to bottom panel of Fig. 8).

Fig. 9 shows the simulated trajectory based on the logged information on the field test on Taylor Glacier, Antarctica. As for the first trajectory on Morteratsch Glacier, we assumed that the logged electrical power P_h is fully converted to the heat flow rate $\dot{Q}_{mh}$ at the melting probe's head and used the same time step for the trajectory model. In contrast to the test on the Morteratsch Glacier, no measurement stops have been made. The trajectory consists of two parts as described in Section 3.2. The first part is the second attempt during the brine sampling mission and the second part is the final attempt to reach the target area. We observe a fairly constant modelled melting velocity of 1.21 m h^{-1} in the first part and of 1.27 m h^{-1} in the second part which is slightly increasing with the run time. This is due to the increasing temperature of the ice and, therefore, less power is needed to heat up the ice to the melting temperature. The measured velocity is varying between 0.8 to 1.2 m h^{-1} with a mean at 1.03 m h^{-1} in the first part and varying between 0.75 m h^{-1} and 1.0 m h^{-1} with a mean value of about 0.90 m h^{-1} in the second part. Here, as discussed earlier, we observe a decreasing trend in the measured melting velocity. Hence, the velocity is here overestimated by about 20% in the first part and about 25% at the beginning of the second part and then increasing with time to about 70% close to the arrival at the target area (compare to bottom panel of Fig. 9).

The modelled melting velocity at the two different glaciers is basically the same and only slightly higher for the temperate Morteratsch Glacier. The contact force of the ice screw was higher at Taylor Glacier. It was about 550 N at Morteratsch Glacier and about 800 N at Taylor Glacier. The increased contact force is probably compensating a little for the lower temperature, but the most important factor for the modelled melting velocity is apparently the used melting power. Furthermore, Fig. 9 shows that the modelled melting velocity is higher the higher the contact force and the warmer the ice is. It is, however, intriguing that the measured velocity shows an opposite behaviour. In the first part of the Taylor Glacier mission, the contact force was lower than in the second part while the velocity was higher in the first part than in the second part. Moreover, the overestimation of melting velocity shows that there are obviously unknown mechanisms for energy losses that are not captured by the model and potentially could explain the discrepancy between modelled and measured melting velocity.

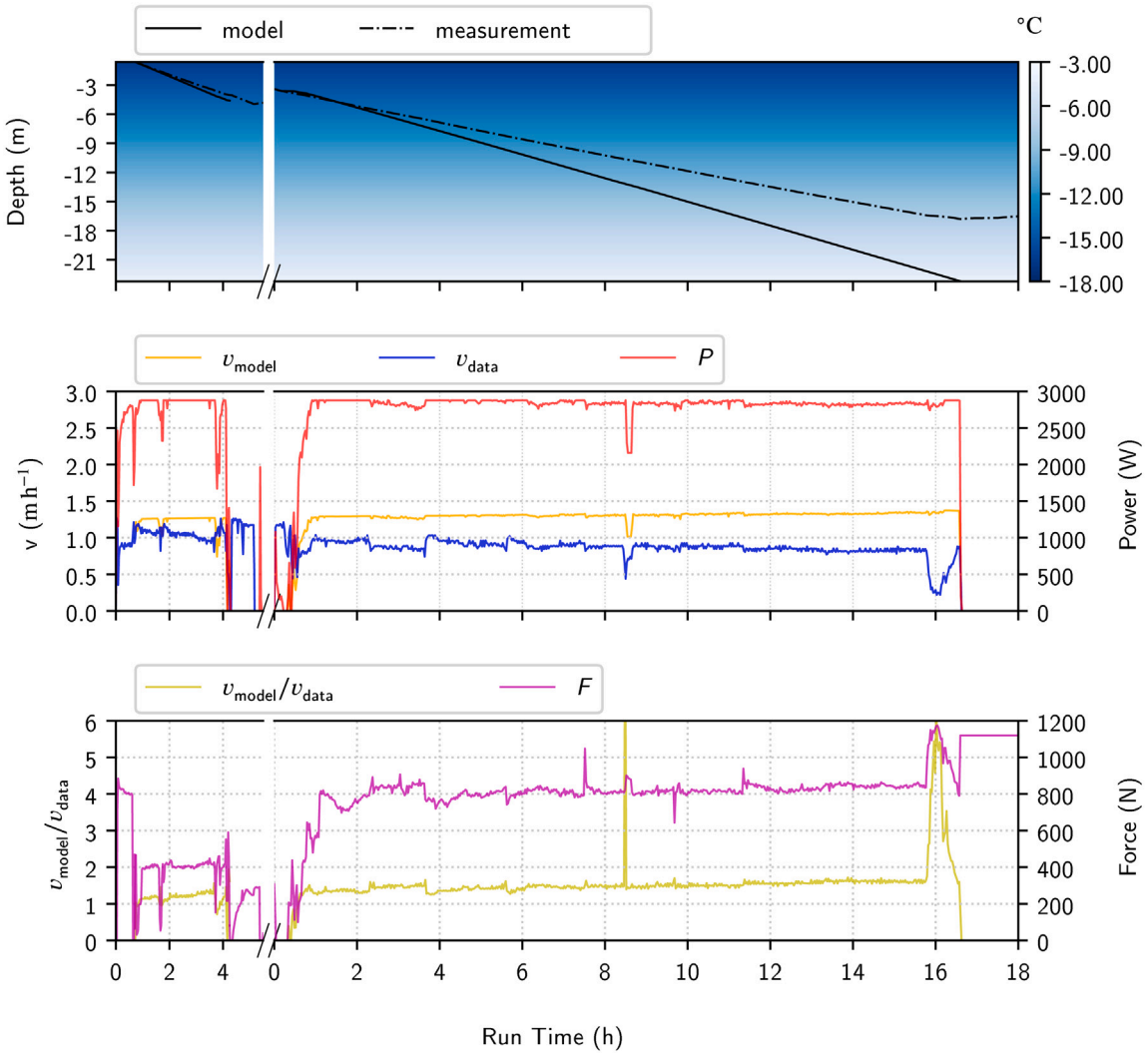

Fig. 9. Trajectory model of field test on Taylor Glacier, Antarctica. The top panel shows the trajectory, i.e. the depth location of the probe as a function of the time both from the logs (measurement) and from the model, while the assumed temperature distribution (here, we assume a linear gradient from −18 °C at the surface (0 m) to −7 °C at a depth of 18 m) is plotted in the background. The centre panel shows the electrical power as well as both the modelled and measured velocity of the melting probe. The bottom panel shows the ratio of modelled to measured velocity of the melting probe. Note that the time axis is broken the first part refers to the second attempt during the brine sampling mission (from 0.72 to 4.25 h) and the second part is the final attempt to reach the target area (from 0.18 to 11.46 h).

6. Discussion

The screw of the IceMole helps to validate trajectory models with field test data, since it provides an independent measure of the distance and its time derivatives without access from the surface. This is especially important in non-temperate ice, where the power cord must be uncoiled from the cryobot itself on long trajectories and therefore would require a cord length measurement device on the probe. Moreover, a hypothetical extraterrestrial probe carrying a power source on board may not rely on determining its travelled distance by cord-length measurement. Yet, ongoing research, for example on both tethered and untethered communication solutions with sufficient robustness and performance for icy moon environments (Patterson et al., 2022; Singh et al., 2023), could also provide means of distance measurement.

The two data sets at hand originate from a navigation technology demonstration and a brine sampling mission, respectively, and were not generated with a focus on efficient probe operation. The consequences become obvious when the modelled required lateral heating power is compared to the actually used supplementary heating power, which was unnecessarily high. Calculations based on the proposed definitions of efficiency reflect the same insight, namely that the probe operated at a lower efficiency than could be achieved with the design under optimal operational parameters. Conversely, the melt process is also modelled incompletely as we only considered one source of heat loss each at the tip and along the probe, respectively. An overestimation of the modelled efficiency is hence expectable even for optimized probe operation, and the deviation increased further because of the high supplementary heating power. Additional uncertainty arises from the square cross-section of the probes used, which is only represented in a simplified way in the models as it was described in Section 4.5. Yet, the arrangement of heating cartridges was selected to minimize the temperature drop in the corners. Moreover, previous research suggest that a decreasing heat flux gradient towards the edges of a melting head could even be beneficial from an efficiency point of view (Schüller and Kowalski, 2017). With respect to side wall heaters, the power density (W m^{-2}) is much lower compared to the melting head. The surface heaters used here extend into the inner corners of the aluminium square tube and the 5 mm material thickness supports sufficient heat transfer even into the corners.

The influence of the contact force has already been investigated from a theoretical point of view (Schüller and Kowalski, 2019; Li et al., 2021; Dachwald et al., 2023). In these works, no ice screw was considered, so that the contact force was simply calculated from the weight of the probe and corrected by the buoyancy. It turned out that

a higher contact force leads to higher melting velocity approaching a certain maximum velocity. A similar investigation yields that the maximum velocity is already reached within a few percent at the contact forces present in the considered field tests.

This premise is supported by the fact that no such effect is visible in the plots of η_{mh} (Fig. 6) and other effects (not covered by the model) seem to dominate the measured efficiency. We therefore consider the measured contact forces on a level for which a further increase does not result in a measurable increase in velocity.

The trajectory model yields results about 15 to 30% above the measured melting speed in the warm ice of Morteratsch Glacier. On the colder Taylor Glacier, the melting speed is overestimated by a factor of 1.35 to 1.5. Hence, the model consistently overestimates the descent velocity of the IceMole in both scenarios. This shows that the assumption that the logged electrical power P_{h} is fully converted to the heat flow rate $\dot{Q}_{\mathrm{mh}}$ does not hold for the field tests and $\dot{Q}_{\mathrm{mh}} < P_{\mathrm{h}}$, which means that there are missing losses not captured by the current model. They have to be identified and included in future extensions to this model. Until then, the trajectory model of Boxberg et al. (2023) gives an upper estimate of the melting velocity.

Also, the heat flux between the heating elements and the tip surface may pose an important source of heat loss. Depending on the type of heating elements and the respective direction of their heat emission, it can be assumed that a certain amount of heat will dissipate into other structural parts of the probe. Introducing these conductive losses to Eqs. (6) and (7) is desirable to improve the model accuracy. Therefore, quantification of these losses with respect to a variety of melting head designs and different heating elements will be subject to subsequent research.

Complementing this study with data from experiments under more controlled conditions and with efficiency-prioritized probe operation enables validation of the trajectory model proposed by Boxberg et al. (2023) with a focus to identify further sources of heat loss as well as the influence of the limiting assumptions of the model. The main limiting assumptions are that (1) the melting probe is always completely surrounded by water, although cracks and crevasses in the ice occur frequently in glaciers and can drain the melt channel, (2) the response to any change in input parameters (e.g., power, temperature, etc.) is instantaneous, (3) no other losses than conductive losses occur, and (4) the melting probe is of a perfectly cylindrical shape. Not all of these assumptions are met by the IceMole and the used data, which gives reasons for a potential mismatch of data and simulation results. The IceMole is not of cylindrical shape. However, we considered an equivalent radius to calculate the melting head area in the simulations to compensate for this. Hysteresis effects occur in reality that are not accounted for in the model, where the response is assumed to be instantaneous. However, this does not affect net energy budget since the hysteresis effect at the start of a melting probe is compensated by the cooldown phase where the melting probe continues melting while the power is switched off. A quantitative investigation of the hysteresis effects is beyond the scope of this work, though. This leaves the mismatch to be explained by losses not covered by our model and the absence or presence of water in the melting channel. From the available field test data, it is not clear whether the melting probe was always surrounded by water or the melt channel was drained during the melting process. Future field tests should account for this and include measurements to quantify the water level and drainage.

Additional experimental data is also required to improve the understanding of supplementary heating requirements in cold ice. While P_{lat} is estimated in the correct order of magnitude, it clearly deviates from the power used in supplementary heaters. But again, a large share of the deviation may be explained by sub-optimal settings of supplementary heaters (e.g., very high side-wall temperatures even during straight melting) and their layout (only two individual heater zones along the 2 m long probe). Nevertheless, efficiency-focused probe operation itself requires improved understanding of a probe's melting behaviour, indicating an iterative approach towards optimal operation.

Confidence on the ice properties, texture and composition of unexplored ice remains another major source of uncertainty. It is evident that the temperature of ice is an important but not the only factor influencing its phase change. In natural terrestrial or extraterrestrial environments, ice is rarely pure, but often contains particulates or dissolved substances in poorly known composition and irregular distribution (Harrison, 1972; Buffo et al., 2020; Vance et al., 2021). Moreover, crevasses, cracks and fractures on a large or small scale can drain the melt water from a melt hole. Depending on the pressure environment, this can reduce the required total heat by decreasing the lateral heat transfer. But they can also increase the required energy in a low atmospheric pressure location like on an icy moon: When an otherwise closed-off melt channel that would enable ice penetration by melting vents off through ice imperfections, the ice must be sublimated instead. Yet, strong tidal and thermal processes make it difficult to estimate the composition and thermal regime of ice crusts (Greenberg et al., 2002; Spencer and Nimmo, 2013).

Our assumption that pure ice was melted in the analysed field tests might therefore also have significant impact on the presented results. However, it is challenging to perform a complete characterization of the ice environment in natural locations (even on Earth) before scientific missions visited these locations. This uncertainty demands not only for more accurate, but in particular also for more robust performance and efficiency models for ice melting probes on the one hand, but, on the other hand, also for robust probe designs.

7. Conclusion

As achieving the targeted performance of a melting probe is a crucial requirement for designing an extraterrestrial melting probe, we investigated the field test performance of an ice melting probe in two terrestrial scientific missions. We described universal measures to improve comparability between different probe designs and validated them by comparing the performance in field-tests with predictions from heat loss models. The comparison revealed, that the actual probe performance matches with the models qualitatively, but quantitatively deviates by 15 to 50%. Our improved model for superposed convective and conductive heat loss reduced the mismatch between results based on model and data, but without having a significant quantitative impact on the deviation.

We conclude three major sources for the deviations between data analysis and model results, which can be treated separately from each other in future research:

1. Operational factors: Unnecessarily high supplementary heating power reduces the actually achieved total efficiency. Comparisons with experiments run with minimum supplementary heating power (e.g., just enough to prevent freezing in) would help to put our results in perspective.
2. Restrictive model assumptions: Our calculations rely on models for convective heat loss at the melting head and lateral conductive heat loss around the full probe, but do not include any other losses. For example, enhanced understanding of heat flow processes between electrical heaters and melting head surface would help to improve the accuracy of η_{mh}. For the superposed heat loss model, a more refined temperature profile in the melt film along the probe and also in lateral direction inside the melt channel could be a step towards better agreement between data and model results. The general formulation of the model allows a simple extension to include further influencing factors.
3. Probe complexity: Idealizations and simplifications are also present in the probe model. For example, it is usually assumed that the entire heat flux provided by the heaters can be used for melting at the tip surface of the probe. But in the IceMole (and

also many other probe designs), electrical heaters have no direct contact with the ice surface. Instead, they are integrated into a melting head fabricated out of copper alloy, which channels the radial heat flow from the electric heating elements towards the ice interface in direction of melting. But at the same time, heat is also conducted into other structural parts of the probe and then no longer contributes to melting.

4. Uncertainties regarding the ice regime: The vertical temperature profile, the amount of water-soluble substances in the ice and amount of particulates of natural ice environments are often poorly known, but can have significant impact on the thermal properties of the ice, as well as on the achievable heat transfer from the melting head into the ice.

These issues directly lead to objectives for future research: Investigating the internal heat flow of specific melting probe designs improves the knowledge on how much of the heater-generated heat flux is actually available at the melting head surface. A transient description of the ice temperature distribution around the heat probe would further refine the required supplementary heating power. This could also take into account the longitudinal and lateral temperature profile in the melt water surrounding the probe in a naturally oversized melt channel. Furthermore, experiments in the field or in the lab with efficiency-focused operational parameters (such as forward or supplementary heating power, contact pressure or surface temperatures) are mandatory for a more accurate assessment of all efficiency models. A reduction in probe complexity, however, must not impair the probe's monitoring capabilities, as precise knowledge about operational parameters should complement more detailed modelling. Rather, models of the internal heat flow for the specific hardware may help to improve the overall model accuracy. Experiment data from well-monitored laboratory environments in a setting similar to those in extraterrestrial ice environments should be carried out to determine the validity of models that were only qualified under terrestrial conditions before. A quantitative study on the accuracy of odometric distance measurement based on the ice screw rotations would further increase confidence in this method. Preliminary results from laboratory experiments investigating distance measurement deviations at different ice temperatures at FH Aachen UAS require further analysis before publication, but already support the suitability of the measurement method. And finally, the influence of impurities and discontinuities of the ice environment on the melting performance should be quantified to allow the estimation of upper and lower limits of the achievable efficiency even for environments that have not been fully explored so far. The model presented here is capable of implementing upgrades in these sectors and should be improved accordingly as soon as results are available.

Declaration of competing interest

The authors declare that they have no known competing financial interests or personal relationships that could have appeared to influence the work reported in this paper.

Data availability

https://doi.org/10.5281/zenodo.6094866.

Acknowledgements

We gratefully acknowledge support through the Explorer Initiatives of the DLR Space Administration funded through the Federal Ministry of Economic Affairs and Energy, Germany, on the basis of a decision by the German Bundestag (50NA1206, 50NA1908, 50NA2009).

References

Aamot, H.W., 1967. Heat Transfer and Performance Analysis of a Thermal Probe for Glaciers. CRREL Technical Report.

Antarctic Treaty Secretatriat, 2018. Management plan for antarctic Specially Protected Area no 172: Lower taylor glacier and blood falls, McMurdo dry valleys, victoria land. URL: https://documents.ats.aq/recatt/att636_e.pdf.

Badgeley, J.A., Pettit, E.C., Carr, C.G., Tulaczyk, S., Mikucki, J.A., Lyons, W.B., 2017. An englacial hydrologic system of brine within a cold glacier: Blood Falls, McMurdo Dry Valleys, Antarctica. J. Glaciol. 1–14. http://dx.doi.org/10.1017/jog.2017.16.

Boledi, L., Key, F., Terschanski, B., Elgeti, S., Kowalski, J., 2023. A scale-coupled numerical method for transient close-contact melting. Comput. Math. Appl. 143 (March), 277–288. http://dx.doi.org/10.1016/j.camwa.2023.05.011.

Boxberg, M.S., Chen, Q., Plesa, A.-C., Kowalski, J., 2023. Ice transit and performance analysis for cryo-robotic subglacial access missions on Earth and Europa. Astrobiology 23, http://dx.doi.org/10.1089/ast.2021.0071.

Buffo, J.J., Schmidt, B.E., Huber, C., Walker, C.C., 2020. Entrainment and dynamics of ocean-derived impurities within Europa's ice shell. J. Geophys. Res.: Planets 125 (10), 1–23. http://dx.doi.org/10.1029/2020JE006394.

Campen, R., Kowalski, J., Lyons, W.B., Tulaczyk, S., Dachwald, B., Pettit, E., Welch, K.A., Mikucki, J.A., 2019. Microbial diversity of an Antarctic subglacial community and high-resolution replicate sampling inform hydrological connectivity in a polar desert. Environ. Microbiol. 21 (7), 2290–2306. http://dx.doi.org/10.1111/1462-2920.14607.

Carslaw, H.S., Jaeger, J.C., 1959. Conduction of Heat in Solids, 2. ed., repr. 2001 ed. In: Oxford Science Publications, Clarendon Press, Oxford [u.a.].

Dachwald, B., Mikucki, J., Tulaczyk, S., Digel, I., Espe, C., Feldmann, M., Francke, G., Kowalski, J., Xu, C., 2014. IceMole: A maneuverable probe for clean in situ analysis and sampling of subsurface ice and subglacial aquatic ecosystems. Ann. Glaciol. 55 (65), 14–22. http://dx.doi.org/10.3189/2014AoG65A004.

Dachwald, B., Ulamec, S., Kowalski, J., Boxberg, M.S., Baader, F., Biele, J., Kömle, N., 2023. Ice melting probes. In: Badescu, V., Zacny, K., Bar-Cohen, Y. (Eds.), Handbook of Space Resources. Springer International Publishing, Cham, pp. 955–996. http://dx.doi.org/10.1007/978-3-030-97913-3_29.

Dachwald, B., Ulamec, S., Postberg, F., Sohl, F., de Vera, J.-P., Waldmann, C., Lorenz, R.D., Zacny, K.A., Hellard, H., Biele, J., et al., 2020. Key technologies and instrumentation for subsurface exploration of ocean worlds. Space Sci. Rev. 216 (5), 1–45.

do Vale Pereira, P., Durka, M.J., Hogan, B.P., Richmond, K., Smith, M.W.E., Winebrenner, D.P., Elam, W.T., Hockman, B.J., Lopez, A., Tanner, N., Moor, J., Ralston, J., Alexander, M., Zimmerman, W., Flannery, N., Kuhl, W., Wielgosz, S., Cahoy, K.L., Cwik, T.A., Stone, W.C., 2023. Experimental validation of cryobot thermal models for the exploration of ocean worlds. Planet. Sci. J. 4 (5), 81. http://dx.doi.org/10.3847/PSJ/acc2b7.

Durka, M.J., Smith, M.W., Ullman, M.J., Cassler, B., Otis, R., Cwik, T.A., Hockman, B.J., Barry, M.M., 2022. Modeling a class of thermal ice probes for accessing the solar system's ocean worlds. Acta Astronaut. 193 (November 2021), 483–495. http://dx.doi.org/10.1016/j.actaastro.2021.12.018.

Feistel, R., Wagner, W., 2006. A new equation of state for H2O ice Ih. J. Phys. Chem. Ref. Data 35 (2), 1021–1047.

Feldmann, M., Francke, G., Espe, C., Chen, Q., Baader, F., Boxberg, M.S., Sustrate, A.-M., Kowalski, J., Dachwald, B., 2023. Performance Data of an Ice-Melting Probe from Field Tests in two Different Ice Environments. Zenodo, http://dx.doi.org/10.5281/zenodo.6094866.

German, L., Mikucki, J.A., Welch, S.A., A., W.K., Lutton, A., Dachwald, B., Kowalski, J., Heinen, D., Feldmann, M., Francke, G., Espe, C., Lyons, W.B., 2021. Validation of sampling antarctic subglacial hypersaline waters with an electrothermal ice melting probe (IceMole) for environmental analytical geochemistry. Int. J. Environ. Anal. Chem. 101 (15), 2654–2667. http://dx.doi.org/10.1080/03067319.2019.1704750.

Greenberg, R., Geissler, P., Hoppa, G., Tufts, B.R., 2002. Tidal-tectonic processes and their implications for the character of Europa's icy crust. Rev. Geophys. 40 (2), 1004. http://dx.doi.org/10.1029/2000RG000096, URL: http://doi.wiley.com/10.1029/2000RG000096.

Harrison, W.D., 1972. Temperature of a temperate glacier. J. Glaciol. 11 (61), 15–29. http://dx.doi.org/10.3189/S0022143000022450.

Haynes, W.M., Lide, D.R., Bruno, T.J., 2017. CRC Handbook of Chemistry and Physics: A Ready-Reference Book of Chemical and Physical Data. CRC Press, Boca Raton, Florida.

Hoffman, M.J., Fountain, A.G., Liston, G.E., 2008. Surface energy balance and melt thresholds over 11 years at Taylor Glacier, Antarctica. J. Geophys. Res. 113 (F4), F04014. http://dx.doi.org/10.1029/2008JF001029.

Kasser, P., 1960. Ein leichter thermischer eisbohrer als hilfsgerät zur installation von ablationsstangen auf gletschern. Geofis. Pura Appl. 45 (1), 97–114.

Kömle, N.I., Tiefenbacher, P., Kahr, A., 2018. Melting probe experiments under Mars surface conditions – the influence of dust layers, CO2-ice and porosity. Icarus 315, 7–19. http://dx.doi.org/10.1016/j.icarus.2018.06.012.

Konstantinidis, K., Flores Martinez, C.L., Dachwald, B., Ohndorf, A., Dykta, P., Bowitz, P., Rudolph, M., Digel, I., Kowalski, J., Voigt, K., Förstner, R., 2015. A lander mission to probe subglacial water on Saturn's moon Enceladus for life. Acta Astronaut. 106, 63–89.

Kowalski, J., Linder, P., Zierke, S., von Wulfen, B., Clemens, J., Konstantinidis, K., Ameres, G., Hoffmann, R., Mikucki, J., Tulaczyk, S., Funke, O., Blandfort, D., Espe, C., Feldmann, M., Francke, G., Hiecker, S., Plescher, E., Schöngarth, S., Schüller, K., Dachwald, B., Digel, I., Artmann, G., Eliseev, D., Heinen, D., Scholz, F., Wiebusch, C., Macht, S., Bestmann, U., Reineking, T., Zetzsche, C., Schill, K., Förstner, R., Niedermeier, H., Szumski, A., Eissfeller, B., Naumann, U., Helbing, K., 2016. Navigation technology for exploration of glacier ice with maneuverable melting probes. Cold Reg. Sci. Technol. 123, 53–70. http://dx.doi.org/10.1016/j.coldregions.2015.11.006.

Li, Y., Talalay, P.G., Fan, X., Li, B., Hong, J., 2021. Modeling of hot-point drilling in ice. Ann. Glaciol. 62 (85–86), 360–373. http://dx.doi.org/10.1017/aog.2021.16.

Li, Y., Talalay, P.G., Sysoev, M.A., Zagorodnov, V.S., Li, X., Fan, X., 2020. Thermal heads for melt drilling to subglacial lakes: Design and testing. Astrobiology 20 (1), 142–156. http://dx.doi.org/10.1089/ast.2019.2103.

Lunine, J., Waite, H., Postberg, F., Spilker, L., Clark, K., 2015. Enceladus life finder: the search for life in a habitable moon. In: EGU General Assembly Conference Abstracts, Vol. 17. pp. EGU2015–14923.

Lyons, W.B., Mikucki, J.A., German, L.A., Welch, K.A., Welch, S.A., Gardner, C.B., Tulaczyk, S.M., Pettit, E.C., Kowalski, J., Dachwald, B., 2019. The geochemistry of englacial brine from taylor glacier, antarctica. J. Geophys. Res.: Biogeosci. 124 (3), 633–648. http://dx.doi.org/10.1029/2018JG004411.

Mikucki, J.A., Auken, E., Tulaczyk, S., Virginia, R.A., Schamper, C., Sørensen, K.I., Doran, P.T., Dugan, H., Foley, N., 2015. Deep groundwater and potential subsurface habitats beneath an Antarctic dry valley. Nature Commun. 6 (1), 6831. http://dx.doi.org/10.1038/ncomms7831.

Nimmo, F., Pappalardo, R.T., 2016. Ocean worlds in the outer solar system. J. Geophys. Res.: Planet. 121 (8), 1378–1399. http://dx.doi.org/10.1002/2016JE005081.

Pappalardo, R., Senske, D., Prockter, L., Paczkowski, B., Vance, S., Rhoden, A., Goldstein, B., Magner, T., Cooke, B., 2015. Science objectives for the Europa Clipper mission concept: Investigating the potential habitability of europa. In: European Planetary Science Congress. pp. EPSC2015–156.

Patterson, W., Craft, K., Lorenz, R., Sequeira, H., Coker, R., Stilwell, R., 2022. An RF concept for communicating with a subsurface cryobot on an ocean world. In: Europlanet Science Congress 2022, 18–23 September. Granada, Spain, pp. EPSC2022–1010.

Philberth, K., 1962. Une méthode pour mesurer les témperatures à l'intérieur d'un Inlandsis. C. R. Acad. Sci. 254 (22), 3881–3883.

Schüller, K., Kowalski, J., 2017. Spatially varying heat flux driven close-contact melting – A Lagrangian approach. Int. J. Heat Mass Transfer 115, 1276–1287. http://dx.doi.org/10.1016/j.ijheatmasstransfer.2017.08.092.

Schüller, K., Kowalski, J., 2019. Melting probe technology for subsurface exploration of extraterrestrial ice – critical refreezing length and the role of gravity. Icarus 317, 1–9. http://dx.doi.org/10.1016/j.icarus.2018.05.022.

Singh, V., McCarthy, C., Silvia, M., Jakuba, M.V., Craft, K.L., Rhoden, A.R., German, C., Koczynski, T.A., 2023. Surviving in ocean worlds: Experimental characterization of fiber optic tethers across Europa-like ice faults and unraveling the sliding behavior of ice. Planet. Sci. J. 4 (1), 1. http://dx.doi.org/10.3847/PSJ/aca3ab.

Sparks, W.B., Schmidt, B.E., McGrath, M.A., Hand, K.P., Spencer, J.R., Cracraft, M., Deustua, S.E., 2017. Active cryovolcanism on Europa? Astrophys. J. Lett. 839 (2), L18.

Spencer, J.R., Barr, A.C., Esposito, L.W., Helfenstein, P., Ingersoll, A.P., Jaumann, R., McKay, C.P., Nimmo, F., Waite, J.H., 2009. Enceladus: An active cryovolcanic satellite. In: Saturn from Cassini-Huygens. Springer, pp. 683–724.

Spencer, J.R., Nimmo, F., 2013. Enceladus: An active ice world in the saturn system. Annu. Rev. Earth Planet. Sci. 41 (1), 693–717. http://dx.doi.org/10.1146/annurev-earth-050212-124025.

Talalay, P., 2014. Perspectives for development of ice-core drilling technology: a discussion. Ann. Glaciol. 55 (68), 339—350. http://dx.doi.org/10.3189/2014AoG68A007.

Talalay, P.G., 2019. Thermal Ice Drilling Technology. In: Springer Geophysics, Springer Singapore, http://dx.doi.org/10.1007/978-981-13-8848-4.

Talalay, P.G., Li, Y., Sysoev, M.A., Hong, J., Li, X., Fan, X., 2019. Thermal tips for ice hot-point drilling: Experiments and preliminary thermal modeling. Cold Reg. Sci. Technol. 160 (January), 97–109. http://dx.doi.org/10.1016/j.coldregions.2019.01.015.

Taylor, B.N., Thompson, A., 2008. The International System of Units (SI). Technical Report, National Institute of Standards and Technology, URL: https://nvlpubs.nist.gov/nistpubs/Legacy/SP/nistspecialpublication330e2008.pdf.

Ulamec, S., Biele, J., Funke, O., Engelhardt, M., 2007. Access to glacial and subglacial environments in the solar system by melting probe technology. Rev. Environ. Sci. Biotechnol. 6 (1), 71–94. http://dx.doi.org/10.1007/s11157-006-9108-x.

Vance, S.D., Journaux, B., Hesse, M., Steinbrügge, G., 2021. The salty secrets of icy ocean worlds. J. Geophys. Res.: Planets 126 (1), 1–5. http://dx.doi.org/10.1029/2020JE006736.

Waldmann, C., Funke, O., 2019. The TRIPLE/nanoAUV initiative a technology development initiative to support astrobiological exploration of ocean worlds. CEAS Space J. http://dx.doi.org/10.1007/s12567-019-00275-7.

Winebrenner, D.P., Elam, W., Miller, V., Carpenter, M., 2013. A thermal ice-melt probe for exploration of earth-analogs to mars, Europa and enceladus. In: 44th Lunar and Planetary Science Conference. http://dx.doi.org/10.1029/2011GL048846, Abstract #2986.